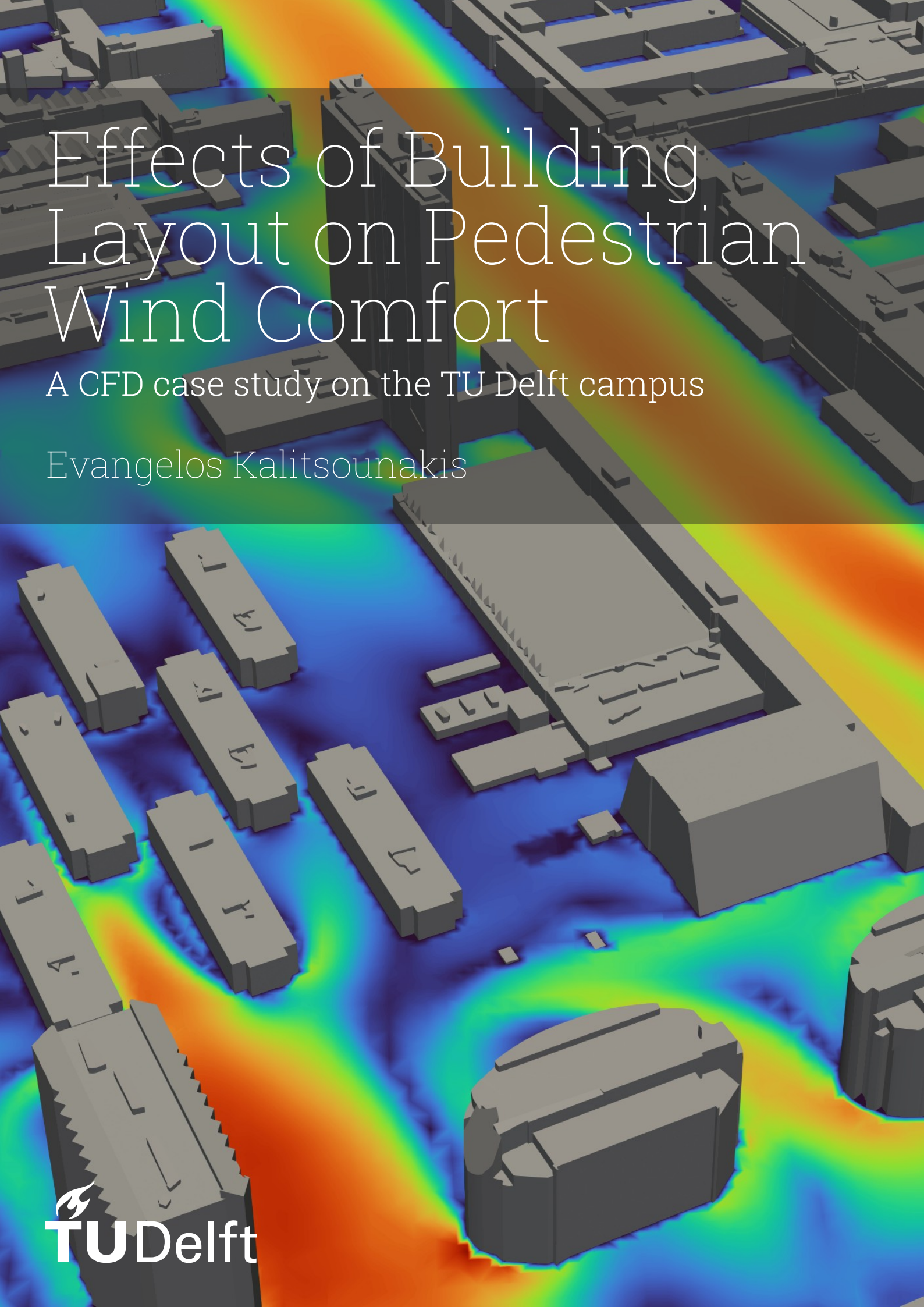

Effects of Building Layout on Pedestrian Wind Comfort

A CFD case study on the TU Delft campus

Evangelos Kalitsounakis

TU Delft

Effects of Building Layout on Pedestrian Wind Comfort

A CFD case study on the TU Delft campus

by

Evangelos Kalitsounakis

Thesis submitted in partial fulfillment of the requirements for the degree of

Master of Science
in
Applied Earth Sciences

Student number: 6052649

Thesis committee:

Dr.ir. S.J.A. (Steven) van der Linden	Chair
Dr. C. (Clara) Garcia Sanchez	Supervisor
Dr. A. Patil	Supervisor
Dr.ir. A.M. (Arjan) Droste	Committee Member

Department of Geosciences & Remote Sensing
Faculty of Civil Engineering and Geosciences, Delft University of Technology
Delft, the Netherlands

Cover: Simulated wind field visualized in ParaView (author's own work)

Preface

This thesis marks the completion of my Master's degree and the end of a meaningful journey.

I would like to sincerely thank my main supervisors, Steven and Clara, for giving me the opportunity to work on this interesting project and for their continuous guidance and valuable feedback throughout this work. I am also especially grateful to Akshay for his constant support and encouragement during the project. Our discussions were a great source of motivation and gave me valuable insights that helped me deliver the best possible version of my work. I also want to thank Arjan for his valuable comments as a member of my thesis committee.

I would also like to thank my friends for always being there along the way. Above all, I am truly thankful to my family for their unconditional support, constant presence and trust in me, without which this experience would not have been the same.

Evangelos Kalitsounakis
Delft, March 2026

Use of generative AI tools

During the preparation of this thesis, the author used large language model (LLM) tools to support language editing, including proofreading, grammatical correction and improvement of phrasing and clarity. LLM tools were also used in a limited way for code-related support, such as improving organization and readability. All scientific reasoning, methodological choices, data analysis, interpretation of results, and final coding decisions were made by the author. All AI-assisted output was carefully reviewed and, where necessary, revised by the author, who takes full responsibility for the final written content of this thesis.

Abstract

Building geometry strongly influences pedestrian comfort and safety, especially in dense urban environments. As urbanization increases and cities continue to develop, understanding how building arrangement affects pedestrian-level wind conditions becomes increasingly important for creating safe and comfortable outdoor conditions. In this thesis, the TU Delft campus was used as a case study to investigate how modifications in the spatial arrangement of buildings affect pedestrian-level wind conditions. By relocating groups of buildings within the campus area, a set of four hypothetical modified layouts was created and steady-state RANS simulations were performed for each layout. To assess pedestrian wind comfort, a combined exceedance criterion based on wind velocity and turbulent kinetic energy was used rather than the standardized wind comfort guideline NEN 8100. The results show that building rearrangement mainly redistributes discomfort zones, following the regions of high wind velocity and turbulence kinetic energy. The strongest effects occur in the places where layout modifications took place. The relocation of high-rise buildings is the dominant factor that determines the probability and the extent of the discomfort zones, with more exposed placements generally leading to a larger area of discomfort. While most layouts mainly redistribute the zones of high discomfort risk, one modified configuration shows the clearest improvement in pedestrian wind comfort in the main central open area of the campus. For a critical wind direction that produces the highest wind speeds in the main open space of the campus, an additional blockage-ratio analysis was performed. The results indicate that local wind velocity in the region responds to upstream geometric blockage, with higher frontal blockage generally associated with lower wind velocity. Overall, these findings highlight the important role of building design in shaping pedestrian-level wind flow and provide useful insight for improving pedestrian comfort in urban spaces.

Contents

Nomenclature

Abbreviations

Abbreviation	Definition
3D BAG	Dutch 3D building model database (3dbag.nl)
ABL	Atmospheric boundary layer
AE	Faculty of Aerospace Engineering (TU Delft)
AHN	National Height Model of the Netherlands (Actueel Hoogtebestand Nederland)
AP	Applied Physics / Faculty of Applied Physics (TU Delft)
AS	Faculty of Applied Sciences (TU Delft)
AULA	Aula Conference Center (TU Delft)
BAG	Basic Registration of Addresses and Buildings (Basisregistratie Adressen en Gebouwen)
CFD	Computational Fluid Dynamics
CEG	Faculty of Civil Engineering and Geosciences (TU Delft)
CityGML	City Geography Markup Language
DNS	Direct Numerical Simulation
EEMCS	Electrical Engineering, Mathematics and Computer Science (TU Delft)
GEM	Gust-equivalent mean (wind speed)
LES	Large-Eddy Simulation
LHS	Latin Hypercube Sampling
LoD	Level of Detail
ME	Faculty of Mechanical Engineering (TU Delft)
NEN	Dutch standard (Nederlandse Norm)
OBJ	Wavefront OBJ geometry file format
PDOK	Dutch national geoportal (Publieke Dienstverlening Op de Kaart)
RANS	Reynolds-Averaged Navier–Stokes
ROI	Region of interest
SW2	Stieltjesweg student housing building (TU Delft)
TKE	Turbulent kinetic energy
TOP10NL	Dutch topographic dataset TOP10NL
TU Delft	Delft University of Technology
WSL	Windows Subsystem for Linux

Symbols

Symbol	Definition	Unit
$A_{\mathrm{blocked}}(x)$	Blocked plan-area used in planar blockage ratio definition	[m^2]
$A_{\mathrm{domain}}(x)$	Domain plan-area used in planar blockage ratio definition	[m^2]
$B_{\mathrm{frontal}}(z)$	Frontal blockage ratio at height z	[–]
B_{mean}	Mean blockage ratio over an upstream section	[–]
$B_{\mathrm{planar}}(x)$	Planar blockage ratio at position x	[–]
C_μ	k–ε model constant ($= 0.09$)	[–]
$C_{\varepsilon 1}$	k–ε model constant ($= 1.44$)	[–]

Symbol	Definition	Unit
$C_{\varepsilon 2}$	k–ε model constant ($= 1.92$)	[–]
d	Displacement height (log-law wind profile)	[m]
g_i	Gravitational acceleration component in direction x_i	[m/s^2]
$H_{\max}$	Maximum building height in the study area/domain	[m]
k	Turbulent kinetic energy (TKE)	[m^2/s^2]
L or L_{up}	Length of upstream section used for blockage averaging	[m]
$L_{\mathrm{blocked}}(z)$	Total blocked width at height z (frontal projection)	[m]
$L_{\mathrm{domain}}(z)$	Total domain width at height z (frontal projection)	[m]
N	Number of samples	[–]
p	Pressure	[Pa]
$\overline{p}$	Time-averaged pressure	[Pa]
P_k	Production of turbulent kinetic energy	[m^2/s^3]
R	Radius of the circular region of interest (ROI)	[m]
t	Time	[s]
$u(z)$	Mean horizontal wind speed at height z (log-law)	[m/s]
u_*	Friction velocity	[m/s]
u_i	Instantaneous velocity component in direction x_i	[m/s]
$\overline{u}_i$	Time-averaged velocity component in direction x_i	[m/s]
u_i'	Fluctuating velocity component in direction x_i	[m/s]
U	Wind velocity magnitude (context-dependent, including averaged magnitude)	[m/s]
U_i	Velocity magnitude for wind direction case i (post-processing)	[m/s]
U_{ref}	Reference wind velocity at z_{ref} (given as 5 m/s at 10 m)	[m/s]
U_{ROI}	Mean wind velocity in the region of interest (ROI)	[m/s]
w	Cross-wind corridor width used for local planar blockage computation	[m]
x_i	Spatial coordinate in direction i	[m]
x', y'	Wind-aligned horizontal coordinates (x' along-wind, y' cross-wind)	[m]
x'_{entry}	Upwind entry location of ROI along x'	[m]
x'_c, y'_c	ROI center coordinates in rotated system	[m]
z	Vertical coordinate / height	[m]
z_0	Aerodynamic roughness length	[m]
z_g	Vertical reference shift used in inlet profiles	[m]
$z_{\min}, z_{\max}$	Minimum/maximum vertical coordinate of the domain	[m]
z_{ref}	Reference height for U_{ref} (given as 10 m)	[m]
ΔU	Difference in averaged normalized velocity field (modified vs reference)	[–]
α	Velocity exceedance threshold parameter	[–]
β	TKE exceedance threshold parameter	[–]
Greek symbols		
δ_{ij}	Kronecker delta	[–]
ε	Turbulent kinetic energy dissipation rate	[m^2/s^3]
κ	von Kármán constant (given as 0.41)	[–]
ν	Kinematic viscosity	[m^2/s]
ν_t	Eddy viscosity	[m^2/s]
ρ	Fluid density (air density)	[kg/m^3]
σ_k	k–ε model constant	[–]
σ_ε	k–ε model constant	[–]

1

Introduction

The quality of outdoor life in urban areas has become a topic of great importance over recent years. Cities constantly face the impacts of climate change, including extreme weather events such as heatwaves, heavy rainfall, and increased drought (Intergovernmental Panel on Climate Change (IPCC), 2021). According to the United Nations, 55% of the global population currently lives in urban areas, and this proportion is projected to increase in the next decades (United Nations, Department of Economic and Social Affairs, Population Division, 2025). As a result, an increasing number of people are on the frontline of climate-related risks. This highlights the need for climate-resilient urban design that ensures comfortable and safe outdoor spaces through an improved understanding of local environmental conditions.

At the same time, as urban centers continue to develop, the built environment forms complex geometries which can further modify the local environment. One of the main drivers of the urban climate is the wind, affecting air quality and pedestrian safety (Britter & Hanna, 2003; Stathopoulos, 2006). Therefore, extensive research has been conducted to examine the influence of urban design on wind flow patterns. Studies primarily focus on the impact of building design, including their height (L. Chen et al., 2017; Zhang et al., 2020), the density (Kubota et al., 2008) and voids between them (Park et al., 2020), showing that city geometry has a strong impact on the flow dynamics. These changes in wind flow are particularly relevant at the pedestrian level, where high wind speeds can lead to discomfort or even unsafe situations, particularly in dense built environments. Studies indicate that wind discomfort or unsafe conditions at the pedestrian level typically arise from local acceleration generated by the interaction between the wind flow and the built environment. Large height differences between the buildings can potentially lead to pedestrian discomfort as they redirect the upcoming wind along the windward face towards the ground. Corner acceleration can also be driven by sharp building edges and sudden changes in facade orientation (Blocken et al., 2016). In addition to the effects of individual buildings, the spatial arrangement also controls the flow. Modifying the relative positioning of buildings can change the path of the flow. Depending on the arrangement, buildings can block and divert the wind or redirect it through the buildings. When the layout increases the blockage along a street, wind speeds at pedestrian level generally decrease due to enhanced sheltering (Stathopoulos & Wu, 1995). On the other hand, configurations that create narrow passages aligned to the wind typically accelerate the flow (Mittal et al., 2018). These effects highlight the strong dependence of local wind conditions on the city geometry. A clear understanding of this relationship is therefore essential for improving wind conditions in urban areas.

TU Delft campus provides a relevant case study to investigate how changes in building arrangement influence wind flow and the pedestrian-level conditions. The campus area contains buildings with varied heights as well as open green spaces and areas with water. These features make it a realistic example of an urban environment. It experiences a very high daily activity, with around 27.000 people on campus every day (TU Delft, 2026). Given the high number of pedestrians and cyclists on the university site, outdoor safety is particularly important, especially in areas where high wind speeds regularly occur. Discomfort and unsafe conditions may arise as the approaching flow is redirected

from the buildings and generates local acceleration. A notable example on the TU Delft campus is the Electrical Engineering, Mathematics, and Computer Science (EEMCS) tower. At about 90 m tall, it is reported to be the second-tallest building in Delft. Due to its height and the significant difference relative to its surroundings, windy conditions lead to strong gusts around the base of the building, which can cause discomfort conditions at the pedestrian level (TU Delft Delta, 2019). As the TU Delft campus continues to develop, new projects regularly modify its layout. A characteristic example is the recent construction of the new Physics building for the Faculty of Applied Sciences in the southern campus area (TU Delft, 2025). Such modifications can alter local wind patterns, and if not systematically investigated, they have the potential to induce unanticipated changes in pedestrian comfort. Understanding these effects is therefore essential for creating a safe and comfortable outdoor environment on campus.

These wind-flow patterns arise from the combined influence of several geometric factors in the building layout, such as variations in building height, the building's exposure to the approaching wind and the spacing between them. Because these factors act simultaneously, the wind field is the outcome of interacting mechanisms, and it is therefore challenging to identify the dominant factors that shape the observed local wind conditions on the campus. A practical way to address this is to isolate the influence of specific layout features by systematically modifying the arrangement of buildings and analyzing the resulting changes in wind flow patterns. This can be achieved through a set of hypothetical layouts in which subsets of buildings are relocated, while the remaining area remains unchanged. Although such modifications of the building's layout in the existing campus are not realistic as actual interventions, investigating hypothetical alterations can provide useful insight into the physical mechanisms that drive the local wind conditions and potential discomfort. Implementing these changes in a real urban environment, such as the TU Delft campus, enables a direct comparison with the existing layout, for which wind-discomfort locations are already known. This allows to identify changes that may improve pedestrian wind comfort in the campus, which is particularly relevant, given the ongoing development projects of the wider campus area.

Urban wind conditions can be studied using experimental approaches, such as field measurements and wind-tunnel experiments, as well as numerical modelling. One of the most widely used methods for urban wind flow prediction is Computational Fluid Dynamics (CFD), which employs numerical techniques to solve the governing equations that describe the fluid. To accurately predict wind flow using CFD simulations, different modeling approaches can be employed, with the Reynolds-Averaged Navier-Stokes (RANS) method being one of the most commonly used. The fundamental principle behind RANS is the application of averaging in time, from which the averaged Navier-Stokes equations are derived. In this framework, the effect of turbulence on the time-averaged flow is modelled in all scales using closure models. The RANS model is widely used in wind studies on urban environments, as it provides a balance between computational efficiency and capability in predictions (Blocken, 2015). Compared to other computational methods, such as Large-Eddy Simulation (LES) or Direct Numerical Simulation (DNS), RANS is significantly less demanding in terms of computational resources, while still providing an accurate representation of the flow field (Patil & García-Sánchez, 2025). Therefore, it is particularly suitable for pedestrian wind comfort assessments, where the main interest lies in the prediction of the mean flow characteristics (Blocken et al., 2016).

1.1. Research scope

The aim of this thesis is to investigate the influence of changes in the building layout on wind flow within the TU Delft campus. Since buildings cannot be physically moved for comparison, the different arrangements considered in this study represent hypothetical layouts, used to provide insight into how variations in urban geometry affect local wind patterns and pedestrian-level wind comfort.

The main research question of this thesis is formulated as follows:

> *How do changes in the spatial arrangement of buildings influence pedestrian-level wind flow patterns on the TU Delft campus?*

To address this main research question, the following sub-questions are defined:

- How does the existing campus geometry affect the wind flow at the pedestrian level?
- How do modifications in building arrangement influence the wind flow patterns, and which areas of the campus experience the most significant changes?
- What are the implications of the observed wind flow patterns for pedestrian wind comfort in each layout?
- How does the building blockage contribute to the observed changes in local pedestrian-level wind flow?

1.2. Thesis outline

The thesis is organized into five chapters.

Chapter 2 provides the theoretical background relevant to this research. It introduces the fundamental principles that describe the urban wind flow and pedestrian-level wind conditions, followed by an overview of Computational Fluid Dynamics (CFD) techniques used for the analysis, based on the existing literature.

Chapter 3 focuses on the methodological framework used in this study. It describes the pre-processing stage, where the simulation input and the computational mesh are created. It also includes the setup of the simulation, including the modeling approach and the selection of boundary conditions. Finally, the steps followed for analyzing the results are described.

Chapter 4 presents the results of the numerical simulations. The simulated wind flow is analyzed for the reference and the modified layouts of the campus by visualizing the simulation outputs. Following this, wind conditions at pedestrian level are examined using wind comfort criteria and selected wind directions are further analyzed to explore the relationship between wind flow and the geometric configuration of the campus. The simulation results are discussed in relation to the research questions and the existing literature.

Chapter 5 summarizes the main conclusions of the study and presents recommendations for future research.

2

Theoretical Background

2.1. Urban wind flow in the built environment

2.1.1. Urban Boundary Layer

The atmospheric boundary layer (ABL) is the the layer of the atmosphere that is in direct contact with Earth's surface (Stull, 1988). As a result, it responds quickly to changes at the surface on short timescales of one hour or less. These may include heat exchange, evaporation, emission of pollutants, and adaptation of flow to local terrain. The depth of the ABL varies in time and space, typically ranging from several hundred meters to a few kilometers. This area is characterized by turbulent flow, which leads to high diurnal variation of the atmospheric variables. Due to the direct interaction with the surface, the structure of the ABL depends on the specific characteristics of the underlying surface.

The lowest part of the ABL, with a depth of approximately 10% of the total ABL depth, is called the surface layer (Stull, 1988). Within the surface layer, the influence of features such as buildings, vegetation, and terrain properties is strongest. (Oke et al., 2017). The charterer of the ABL varies between daytime and nighttime conditions in response to the daily solar cycle. During the daytime, the surface heating increases the turbulence, leading to a mixed layer which is typically higher compared to the surrounding rural area. In this layer, the mixing results in a relatively uniform vertical distribution of the variables that describe the flow, such as the wind speed, temperature and humidity. In the night, as the heating from the surface stops, a nocturnal stable layer forms near the ground. This layer is characterized by low turbulence, resulting in a flow that is decoupled from the surface. Above this layer, the daytime mixed layer transforms into a residual layer, with the characteristics of the previous well-mixed layer (Stull, 1988).

Above urban areas, the ABL adapts to the layer directly affected by roughness elements, referred to as the urban canopy, leading to the development of a characteristic vertical structure known as the urban ABL (Oke et al., 2017). The urban ABL can be divided into different sub-layers, as illustrated in Figure 2.1. Close to the ground, the flow exhibits a complex behavior, due to the built environment. As seen from the Figure 2.1, the surface layer can be further divided into parts: the roughness sublayer and the inertial sublayer (Oke et al., 2017). The roughness sublayer is the lower part of the surface layer, extending from the ground up to 1.5 to 3 times the height of the urban elements. In this part, the flow is strongly influenced by individual elements of the urban environment. As the roughness of the surface increases, the roughness sublayer becomes deeper. The lowest part of the urban boundary layer, extending up to approximately the mean building height, is the urban canopy layer (Oke et al., 2017). This layer exhibits microscale flow processes with strong spatial and temporal variability. Typical flow features include local updrafts and downdrafts, flow overturning, vortices (Oke et al., 2017).

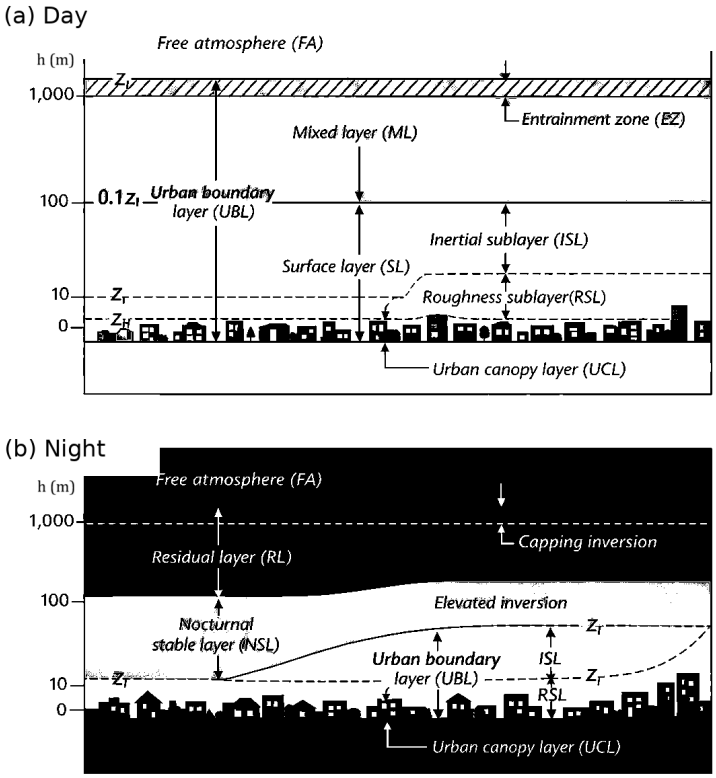

Figure 2.1: Representation of the vertical structure of the urban ABL (adapted from Oke et al., 2017).

In the surface layer, under neutral conditions, the mean horizontal wind speed profile in the vertical direction can be described using the logarithmic law (Britter & Hanna, 2003).

$$u(z) = \frac{u_*}{\kappa} \ln\left(\frac{z-d}{z_0}\right), \tag{2.1}$$

where u_* is the friction velocity, κ is the von Kármán constant, z_0 is the aerodynamic roughness length, and d is the displacement height.

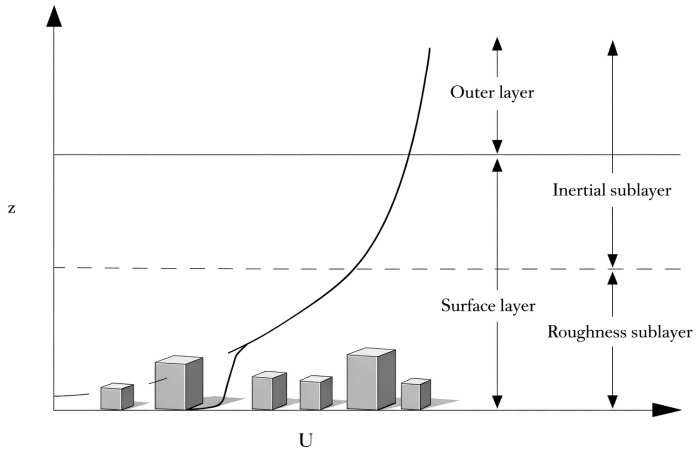

Figure 2.2: Schematic representation of the vertical distribution of the wind speed profile in ABL (adapted from Britter and Hanna, 2003).

2.1.2. Typical wind effects in the urban environment

The logarithmic profile in Eq. (2.1) provides a representation of the mean horizontal wind profile and defines the boundary conditions at the inlet side in numerical models (Richards & Hoxey, 1993). However, in the surface layer, the flow exhibits a much more complex behavior due to the presence of urban elements, such as buildings and vegetation. As the approaching air is blocked by obstacles, it is forced to flow around and between them, creating regions with different speeds and directions. These localized effects arise from the interaction of the flow with both individual buildings and groups of buildings.

Individual building

As the wind approaches a building, the flow in front of the windward face decelerates and a high-pressure displacement region forms. In this region a stagnation point occurs, where the local velocity of the flow is close to zero and the pressure becomes maximum. From this point, the flow is diverted up over the roof, around the sides and down the windward side of the building, toward the ground. This downward directed flow along the windward side of the building, commonly referred to as downwash, increases the wind velocity near the ground. At pedestrian height this redirected flow can locally be experienced as wind coming from the building facade, rather than from the dominant wind direction, which may be experienced as counterintuitive. The downwash can detach from the building before it reaches the ground and then turn upward, generating a vortex that extends downstream on both sides of the building (ASHRAE, 2005). Additional corner vortices can form near the windward edges. On the roof, the wind is locally accelerated, as the streamlines are compressed. Flow separation can occur, forming a separated shear layer above the roof and a recirculating region. Behind the building, the separated flow from the roof and side edges creates a region of low pressure. This results in a cavity region on leeward face. The wind speed in the cavity is reduced compared to the approaching flow, creating a sheltered zone while near the ground, the wind profile can experience return of the flow toward the building (Oke et al., 2017).

The main flow patterns around an isolated building are illustrated in Figure 2.3

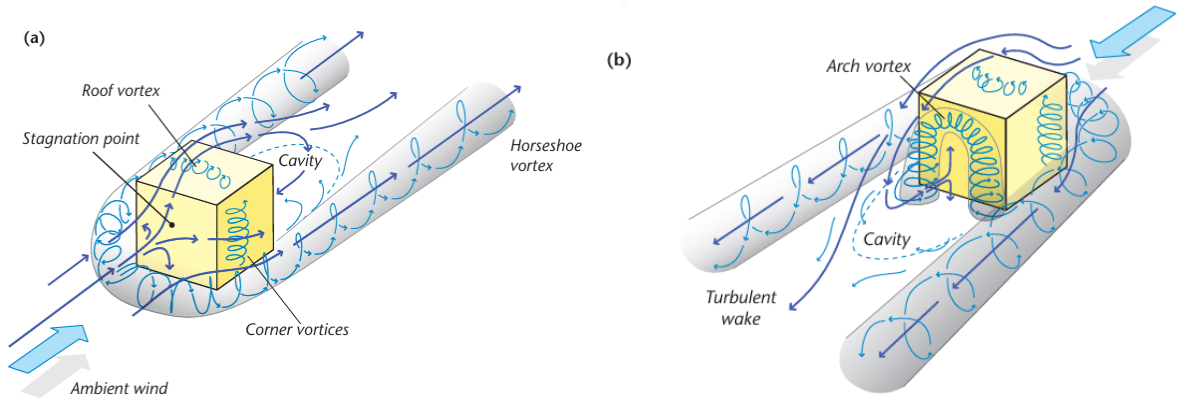

(a) Windward-side view. **(b)** Leeward-side view.

Figure 2.3: Main flow patterns around an isolated building (source:Oke et al., 2017).

Group of buildings

In urban environments, buildings are rarely isolated. Instead, multiple buildings with different shapes, heights and spatial arrangements are present. This has a strong influence on the local wind conditions, leading to spatial variability in wind speed and direction.

Rows of buildings, parallel to each other, along streets form open corridors that are commonly referred to as street canyons. In these regions, as the wind is constrained by building facades, it creates different patterns that depend on the incident angle of the flow.

When the approaching wind is approximately perpendicular to the street canyon, the flow inside a street canyon typically forms a recirculation vortex. This vortex is driven by flow separation at the roof of the

building and is reinforced by downward flow along the downwind canyon wall, although its structure and strength depend on the canyon aspect ratio. This can lead to high wind velocities in the canyon, with higher speeds occurring in the upstream corners of the buildings (To & Lam, 1995). In cases where taller buildings are placed downwind of lower ones, the wind is redirected to the ground level, leading to stronger wind conditions between the buildings (Adamek et al., 2017). If the approaching wind is more aligned with the canyon axis, the recirculating vortex becomes weaker, and the wind flows mainly along the canyon. In cases where the width of the canyon is narrow relative to the height of the buildings, wind speed can increase. This flow pattern is often described as channelling. The intensity of this phenomenon depends on the canyon geometry. In converging passages between buildings, the strongest wind occurs for the narrowest passage and decreases as the width increases (Mittal et al., 2018). Height variation along the street canyon also affects the flow patterns and the wind conditions at the pedestrian level. More specifically, step-up canyons, where building height increases in the downwind direction, generally promote stronger mixing of the flow and therefore provide higher ventilation than canyons with buildings at equal height and step-down canyons, where building height decreases in the downwind direction. (Baş et al., 2024).

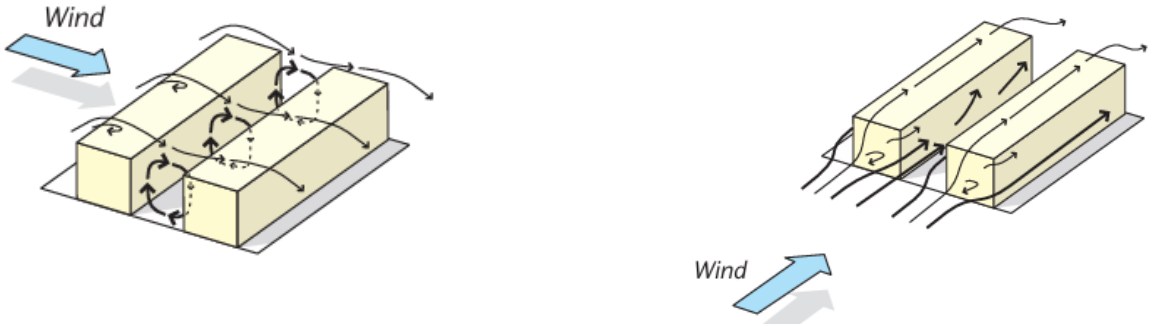

(a) Approaching wind approximately perpendicular to the canyon axis : cross-canyon recirculation vortex.

(b) Approaching wind approximately aligned with the canyon axis: channelling along the canyon (possible jetting near the entrance).

Figure 2.4: Typical street-canyon flow regimes for different approach wind directions (adapted from Oke et al., 2017).

In addition to street-canyon effects, local wind acceleration can occur in locations where the space between the buildings becomes narrow across the wind direction. The increase in speed is caused by the so-called Venturi effect, and it is typically stronger in the bottleneck.

Behind buildings, flow separation can create wake zones where the wind speed is reduced. These sheltered regions depends strongly on the overall arrangement of buildings. Configurations that include a square central open space, with the windward side opened toward the prevailing wind direction, have been reported to provide better wind conditions at the pedestrian level. (Mittal et al., 2018).

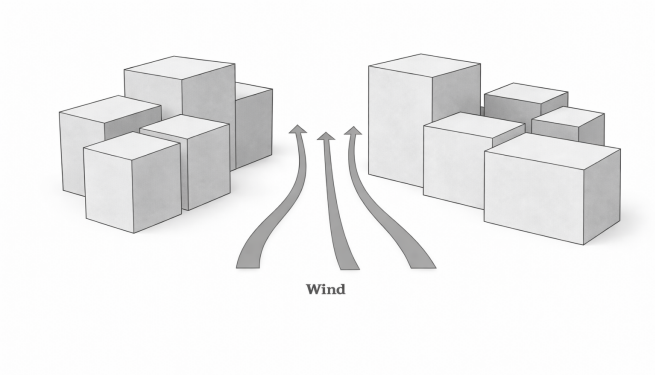

Figure 2.5: Schematic representation of Venturi effect.

In dense building environments, building arrangements can create enclosed spaces, such as courtyards. Depending on the size and the surrounding building height, the approaching wind may either penetrate into the space or pass mainly above roof level, resulting in sheltered regions with low mean wind speeds (Mittal et al., 2018).

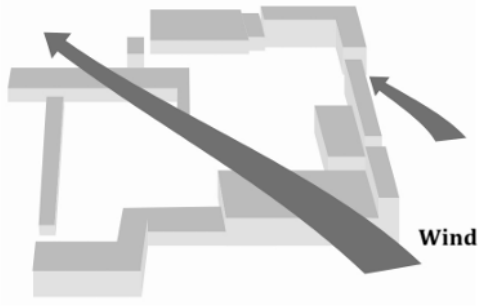

Figure 2.6: Mesh effect (adapted from Reiter, 2010).

The mechanisms described above represent simplified flow patterns that commonly occur around buildings. In practice, the resulting wind field in urban areas is a combination of individual building effects and effects driven from group of buildings. Buildings are often arranged in complex irregular configurations, with variations in height, shape and orientation. Moreover additional elements, such as variations in surface roughness and local topographic features further modify the flow, leading to complex local wind conditions.

2.2. Pedestrian-level wind conditions

The outdoor human comfort in urban climates is dependent on several factors, including the wind speed, air temperature, relative humidity and solar radiation (Stathopoulos, 2006). In order to identify locations where wind conditions may lead to discomfort or unsafe conditions for people, several pedestrian wind comfort criteria have been applied (Blocken et al., 2016). These criteria evaluate comfort based on the frequency that wind speed exceeds certain specified wind speed levels over time. These levels correspond to certain pedestrian activities, such as sitting, standing, or walking. Comfort is then determined by the probability of local wind speeds exceeding these levels. The criteria differ mainly in the definition of the wind speed. Some approaches, such as the Lawson criterion (Lawson, 1978) and Dutch standard NEN 8100 (NEN, 2006) are based on mean wind speed while others, such as the City of London wind microclimate guidelines (City of London Corporation, 2019) and comfort criterion by Melbourne (Melbourne, 1978), also account for wind gusts.

To provide a reference scale for the comfort categories, Table 2.1 presents the classification used in the City of London wind microclimate guidance (City of London Corporation, 2019). The guideline is based on a Lawson classification, expressing the wind thresholds in terms of mean and gust-equivalent mean (GEM) wind speed. Here, the mean wind speed refers to the time-averaged flow, typically averaged over 10–15 minutes, while the GEM represents a mean-speed equivalent that includes the effect of gustiness, obtained by converting gust values into an equivalent mean wind speed. This classification is provided as a reference for the comfort levels. In this study, the criterion adopted to access the wind comfort is described in the methodology chapter.

Table 2.1: Wind comfort and safety categories from the City of London wind microclimate guidance. Reproduced from City of London Corporation, 2019.

Category	Mean & GEM wind speed (5% exceedance) (m/s)	Description
Frequent sitting	2.5	Acceptable for frequent outdoor sitting use, e.g., restaurants, cafés.
Occasional sitting	4.0	Acceptable for occasional outdoor sitting use, e.g., general public outdoor spaces, balconies, and terraces intended for occasional use.
Standing	6.0	Acceptable for entrances, bus stops, covered walkways, or passageways beneath buildings.
Walking	8.0	Acceptable for external pavements and walkways.
Uncomfortable	> 8.0	Not comfortable for regular pedestrian access.
Unsafe	15.0	Presents a safety risk for pedestrians.

Recent studies show that pedestrian-level wind conditions are strongly affected by building geometry (Mittal et al., 2018), including the effects of the buildings height, the shape and the spatial arrangement. Taller buildings can significantly affect the wind flow at pedestrian height, as a result of strong downwash which transfers wind from higher heights to the ground. This tends to lead to high wind speed conditions around the building at pedestrian height, but increases the local ventilation (Adamek et al., 2017; Mittal et al., 2018). This effect can be even more pronounced, when the building is isolated, with studies showing higher maximum wind speeds at pedestrian level compared to when the same building is placed in a regular urban area (Zhang et al., 2020). Increasing building width generally blocks the incoming wind, creating sheltered regions with lower speeds (Mittal et al., 2018). The magnitude and spatial extent of these high-speed regions are also sensitive to geometric details, such as height variations and building roof shape. Comparisons between simplified and more detailed building representations indicate that these features can affect pedestrian-level wind (Patil & García-Sánchez, 2025).

In addition to height, the shape of a building has an impact on the wind conditions. Sharp corners tend to produce stronger corner acceleration. As a result, corner modifications can reduce the areas around buildings that experience wind discomfort. Increasing building width generally blocks the incoming wind, creating sheltered regions with lower speeds (Mittal et al., 2018).

As discussed in Section 2.1.2, the urban layout is a key factor that determines the wind conditions in the area. The arrangement of buildings controls how the wind is guided through streets, passages, and intersections around the buildings. Even in simple urban settings, studies report that the resulting flow field can be complex and very difficult to predict (Soulhac et al., 2009). Wind discomfort is usually associated with narrow passages, where the flow locally accelerates, creating channelling. The impact of building arrangement and height variation has also been examined. Results in wind-tunnel studies show that wind speeds along streets decrease as the blockage ratio increases while the maximum wind speed increases with the height difference between the reference building and its surroundings (Stathopoulos & Wu, 1995).

2.3. CFD approaches for urban wind studies

For a continuous, incompressible Newtonian fluid, the flow is described by the continuity equation and Navier–Stokes equations, which represent conservation of mass and momentum in the flow. In differential form they are written as:

$$\frac{\partial u_i}{\partial x_i} = 0, \tag{2.2}$$

and

$$\frac{\partial u_i}{\partial t} + u_j \frac{\partial u_i}{\partial x_j} = -\frac{1}{\rho}\frac{\partial p}{\partial x_i} + \nu \frac{\partial^2 u_i}{\partial x_j \, \partial x_j}, \tag{2.3}$$

where u_i is the instantaneous velocity component in direction x_i, p is the pressure [kg m^{-1} s^{-2}], ρ is the fluid density [kg m^{-3}] and ν is the kinematic viscosity [m^2 s^{-1}]. These equations form a system of nonlinear partial differential equations for the velocity field u_i and the pressure field p, describing incompressible Newtonian flow.

The Navier–Stokes equations describe the fluid motion, however the nonlinear convective term makes the general three dimensional case fundamentally challenging. In particular, there is no general proof that smooth solutions exist globally in time. For most geometries and boundary conditions, the Navier-Stokes equations do not have an analytical solution, so they are solved numerically.

Main CFD methods

In many practical applications, the flow is also turbulent, leading to variations in the flow field in a wide range of spatial and temporal scales. To simulate turbulent flows, different CFD approaches can be used, depending on the extent to which turbulence is resolved or modelled. Main groups of CFD approaches include:

- Direct Numerical Simulation (DNS)
- Large-Eddy Simulation (LES)
- Reynolds-Averaged Navier–Stokes (RANS)

DNS resolves the full range of turbulence scales. Since all relevant flow motions are resolved directly, it provides the most accurate representation of the flow. However, resolving these smallest scales requires extremely fine mesh resolution in the domain and very small time steps to capture the smallest turbulent scales. This leads to a very high computational cost, which makes it unfeasible for urban wind comfort studies.

LES resolves the large turbulent motions of the flow and models scales under a particular length scale, which is typically taken to be the grid resolution. Hence, the term subgrid model is usually applied. This method can provide accurate predictions of the flow and shows a strong agreement with field measurements (van Hooff et al., 2017). One major practical limitation in LES setups is the computational cost associated with resolving unsteady turbulent motions and detailed building geometry. Although finer geometric detail can in principle be modeled, it requires a finer mesh and smaller time steps, which rapidly increase the computational resources. As a result, the geometric resolution that can typically be afforded is often on the order of meters in the horizontal plane (Keskinen & Hellsten, 2025). This can filter out small-scale geometric effects, which have been shown to have a large effect on the flow (Patil & García-Sánchez, 2025).

The RANS approach solves for time-averaged quantities and models turbulence in all scales using closure models. Despite the lower accuracy of RANS compared to LES, it is significantly more computationally efficient. Wind comfort assessments typically require simulations for multiple inflow directions which makes computational efficiency a primary constraint. As a result, RANS has been widely used for wind comfort studies, as it provides a good balance between the ability to predict the main mean-flow features at pedestrian level and computational efficiency (Blocken et al., 2016; Mittal et al., 2018).

RANS is widely used as a standard engineering approach in pedestrian wind comfort studies. Given that the thesis also considers multiple layouts, with 12 inflow directions per layout, a large number of CFD runs is required. Given its suitability for this application, together with its computational efficiency, RANS was considered an appropriate choice for the present study.

RANS formulation and turbulence closure

RANS is based on a statistical description of the flow, where variables are decomposed into a mean and a fluctuating component (Reynolds decomposition):

$$u_i = \overline{u_i} + u_i', \tag{2.4}$$

$$p = \overline{p} + p'. \tag{2.5}$$

Here, $\overline{(\cdot)}$ denotes the average in time of a quantity and $(\cdot)'$ is the turbulent fluctuation. This decomposition assumes that all fluctuations on the average state are therefore the result of turbulence.

The Reynolds-averaged Navier-Stokes equations are obtained by substitution of this decomposition in the standard Navier-Stokes equations and subsequently averaging over time. The final RANS equations are:

$$\frac{\partial \overline{u_i}}{\partial x_i} = 0, \tag{2.6}$$

$$\frac{\partial \overline{u_i}}{\partial t} + \overline{u_j}\frac{\partial \overline{u_i}}{\partial x_j} = -\frac{1}{\rho}\frac{\partial \overline{p}}{\partial x_i} + \nu\frac{\partial^2 \overline{u_i}}{\partial x_j \partial x_j} - \frac{\partial \overline{u_i' u_j'}}{\partial x_j}. \tag{2.7}$$

The additional term $\overline{u_i' u_j'}$ arises from averaging the nonlinear convective term in the equation and it is called Reynolds stress tensor. They are referred to as stress because it acts as an additional stress term, analogous to viscous stress. Physically, it represents the transport of momentum caused by turbulent velocity fluctuations (Kundu et al., 2012). Since this term introduces new unknowns, the system is not closed and requires a turbulence closure model (Launder & Spalding, 1974).

In practice, RANS turbulence closures can be grouped into two broad categories: eddy-viscosity models, which approximate the Reynolds stresses using a turbulent (eddy) viscosity, and Reynolds-stress models, which solve additional transport equations for the Reynolds stresses directly.

Eddy-viscosity models (e.g., k–ε and k–ω) are commonly used in engineering applications (Launder & Spalding, 1974). They use the Boussinesq hypothesis to relate the Reynolds stresses to the mean strain-rate tensor through an isotropic turbulent viscosity:

$$-\overline{u_i' u_j'} = \nu_t \left(\frac{\partial \overline{u_i}}{\partial x_j} + \frac{\partial \overline{u_j}}{\partial x_i} \right) - \frac{2}{3} k\, \delta_{ij}, \tag{2.8}$$

where ν_t is the eddy viscosity, k is the turbulent kinetic energy, and δ_{ij} is the Kronecker delta (Launder & Spalding, 1974).

3

Methodology

This chapter includes the methodology of the thesis. It first presents an overview of the overall workflow and then describes in detail all the individual steps followed in the thesis.

3.1. Research workflow

The workflow, presented in Figure 3.1, shows the overall structure of the study, including all the main steps followed during the thesis. It is divided into three major phases: *Pre-processing*, in which the simulation inputs are prepared; *Simulation run*, where the numerical model is executed; and finally *Analysis*, where the simulation results are analyzed. Each one of these consists of several tasks.

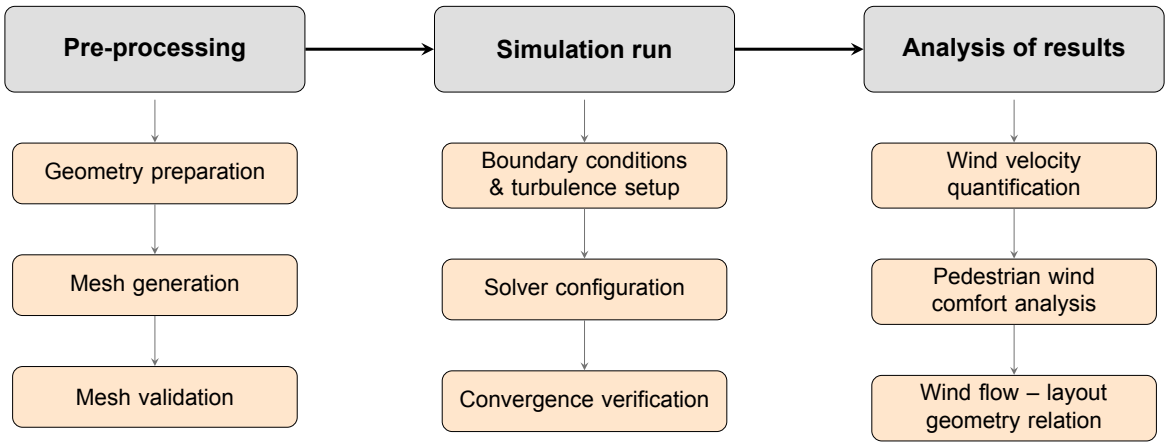

Figure 3.1: Overview of the workflow. The grey boxes indicate the main workflow stages, while the orange boxes correspond to sub-tasks within each stage.

3.2. Pre-processing

In order to perform the simulations, the correct input needs to be created. This pre-processing stage consists of three main steps: preparation of the geometry (including definition of the study area, geometry construction and modification), mesh generation and mesh validation. The analytical description of these steps is presented in this chapter.

3.2.1. Study area: TU Delft campus

The study area selected for this research is the campus of Delft University of Technology (*TU Delft campus*) in Delft, Netherlands. The domain extends over an area of approximately $1\ \mathrm{km}$ by $1\ \mathrm{km}$, including both the main campus and the surrounding residential area. The topography of the terrain is relatively flat, with elevation ranging from $-5\ \mathrm{m}$ to $+7\ \mathrm{m}$ relative to sea level (OpenStreetMap contributors, 2026). The area represents a typical urban environment, consisting of built-up areas, as well as green spaces and small areas of water.

The campus layout is characterized by an open spatial arrangement, with two parallel rows of buildings oriented approximately $155°$, measured clockwise from north. In the central area between these buildings, there is a large open green space, along the same direction, with scattered low vegetation and trees. The area of the campus is surrounded by residential blocks, arranged in a structured grid, and a canal runs on the western side. Most of the buildings can be classified as low- or middle-rise, but there are also some high structures (Stewart & Oke, 2012). The tallest buildings are the faculty of Electrical Engineering, Mathematics and Computer Science (EEMCS; 90m) and the Stieltjesweg student housing building (SW2; 71m), located in the center of the campus and the faculty of Aerospace Engineering (AE; 53m) in the southern part of the campus. Other large buildings include the faculties of Civil Engineering and Geosciences (CEG), Mechanical Engineering (ME), Applied Physics (AP), Applied Sciences (AS) and the Architecture and the Built Environment (Arch), as well as the Aula Conference Center and the TU Delft Library. Figure 3.2 shows an overview of the central area of TU Delft campus, including the names of the main buildings.

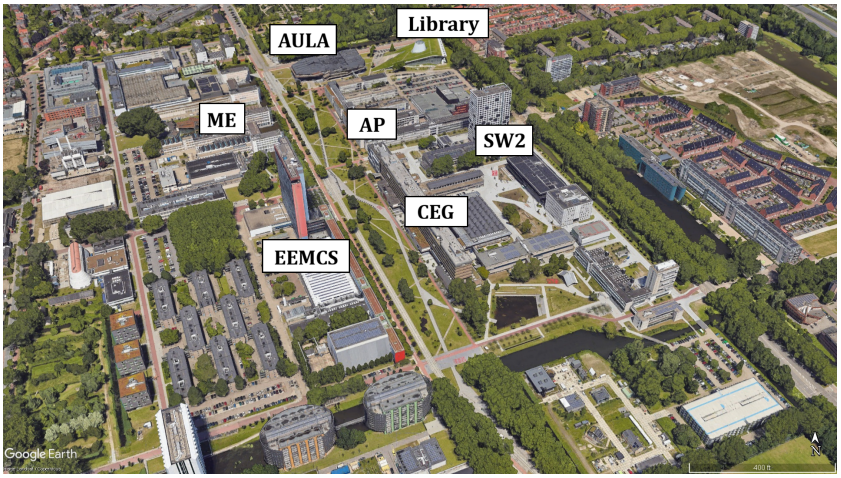

Figure 3.2: Overview of the TU Delft campus (source:Google Earth, 2025). The figure focuses on the central part of the campus, with labels included for the buildings. The AE and AS buildings lie outside the displayed area.

3.2.2. Geometry construction

In order to perform the CFD simulations, a detailed 3D model of the urban environment needs to be constructed. This 3D model contains the spatial information of the computational domain, using vector-based geometric data. It is typically composed of different elements, each corresponding to different components of the built environment (e.g., buildings, roads, trees). Each of these elements has its own geometry, which can be modeled with varying complexity. The amount of detail used in the geometry to represent the real structures is referred to as Level of Detail (LoD), as defined by Open Geospatial Consortium (2012). This concept can be applied in several elements of the urban area, however, it is primarily used in buildings. A brief overview of the different LoDs for buildings geometry is given below:

- LoD0: provides footprints and basic height information of the buildings.
- LoD1: consists of simple block models with only horizontal and vertical faces and it usually has a uniform height.

- LoD2: models buildings as structures with simplified roof geometries, offering a more realistic exterior shape.
- LoD3: contains a more detailed representation of the building, including openings (i.e. windows, doors), balconies, more detailed roof structures and facade elements.

When performing CFD simulations, the level of detail is a very important aspect in the 3D model, as it affects the capability of the simulation to describe the flow (Patil & García-Sánchez, 2025). Previous studies have shown that differences in geometric detail can lead to variations in the simulated wind field (Hågbo et al., 2021), with the most noticeable deviations in wind velocity typically observed around tall structures (García-Sánchez et al., 2021). Choosing the appropriate level of geometric detail depends on the computational resources required to construct the model, but also on the demands of the specific application.

In this study the 3D model of the TU Delft campus was created using four geometric datasets: *buildings*, *terrain*, *vegetation*, and *water bodies*. Including these components in the simulations, allows to capture the effect of the different types of terrain, leading to a better representation of the building environment. The buildings are represented by 3D solids while the different types of terrain are modeled as surfaces.

The building dataset was obtained from the *3D BAG* (3dbag.nl), a database which provides detailed three-dimensional building models for the Netherlands (Peters et al., 2022). These models are generated using open data sources, such as the *Basic Registration of Addresses and Buildings* (BAG), the *National Height Model of the Netherlands* (AHN) digital elevation data and the TOP10NL dataset, part of the Topographic Register of the Netherlands. 3D BAG uses a refined LoD specification for the geometry of the buildings, known as *improved Level of Detail (LoD) specification*, proposed by Biljecki et al. (2016), the schematic representation of which is shown in Figure 3.3.

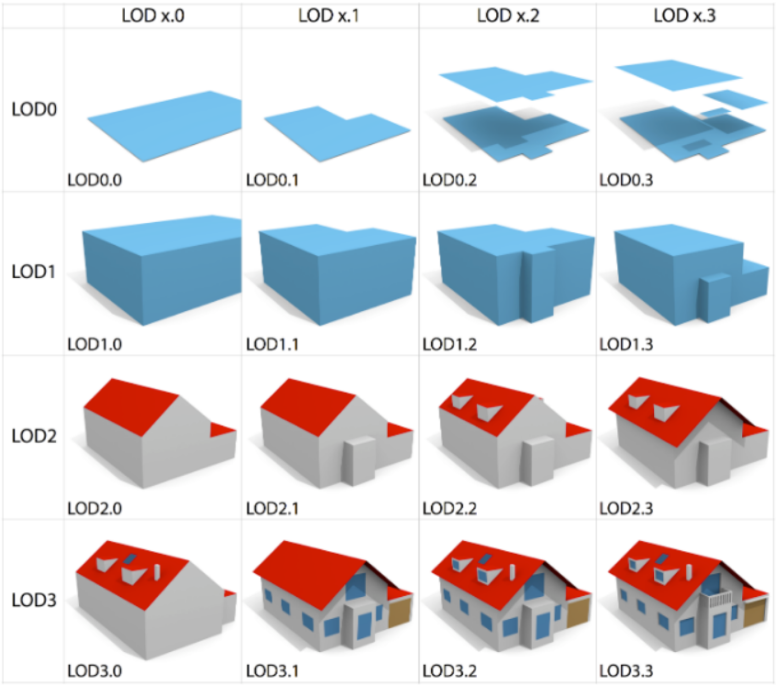

Figure 3.3: Schematic illustration of the different Levels of Detail
Source: adapted from Biljecki, F., Ledoux, H., & Stoter, J. (2016).

This scheme divides each of the standard CityGML LoD0–LoD3 into four subcategories, resulting in 16 possible LoDs. There are three LoDs available in 3D BAG database: LoD 1.2, LoD 1.3, and LoD2.2. For this work, LoD 2.2 was selected for the buildings, since, it can provide a more accurate representation of the geometry and results to more realistic wind fields, compared to lower LoDs (García-Sánchez et al., 2021). The surface datasets for terrain, vegetation and water were derived from the Dutch national geoportal (www.PDOK.nl).

The geometry datasets for this study were provided as preprocessed geometry inputs in `Wavefront OBJ` format, already in a common local coordinate system. In the .obj files the geometry is stored as a text-based structure. The files consist of two types of entries: `v`-lines, in the form `v x y z`, defining the coordinates of each vertex and `f`-lines, which represent surface faces, based on the defined vertices. As a result, in each file the entire geometry is represented as a surface mesh. The building dataset covers an area of approximately $2\ \mathrm{km} \times 2\ \mathrm{km}$, while the terrain, vegetation, and water-surface datasets extend over a larger region of about $7.6\ \mathrm{km}$ in both horizontal directions. The vertical extent is relatively small, ranging from approximately 10 to $13\ \mathrm{m}$ for the surface datasets and up to nearly $100\ \mathrm{m}$ for the buildings. The domain dimensions are summarised in Table 3.1.

Table 3.1: Spatial range of the geometry datasets.

Dataset	**Spatial range (m)**		
	X	**Y**	**Z**
Buildings	1971.6	2085.0	99.2
Terrain	7642.9	7642.9	12.6
Vegetation	7623.0	7617.9	12.8
Water bodies	7626.2	7612.9	9.0

The spatial ranges of the datasets in Table 3.1 correspond to the final reconstructed geometry used for the simulations. These datasets were provided as preprocessed in common local coordinate system.

An overview of the domain around TU Delft campus is shown in Figure 3.4. The datasets were visualised in ParaView, with colours representing the different geometric components: buildings, vegetation, water bodies and terrain.

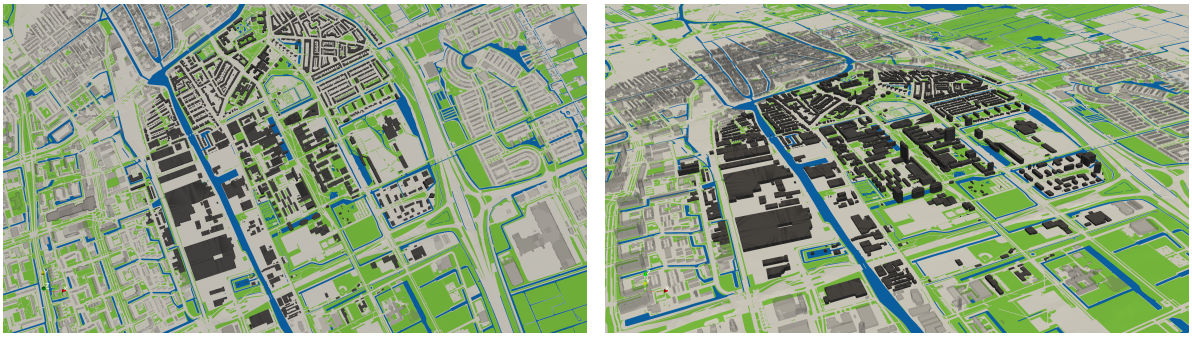

(a) Top view. **(b)** Perspective view.

Figure 3.4: 3D geometry visualised in *ParaView.* The colours represent the geometric components: buildings (dark grey), vegetation (green), water bodies (blue), and terrain (light grey).

3.2.3. Geometry modification

The area displayed in Figure 3.4 provides the reference configuration of the existing TU Delft campus. For a clearer view of the spatial arrangements of the buildings, Figure 3.5 presents the building footprints of the study area.

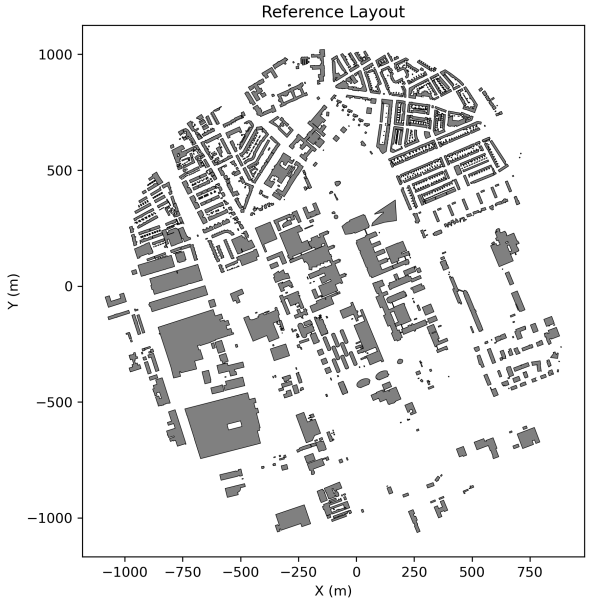

Figure 3.5: Reference layout in plan view. Unchanged building footprints are shown in grey, and relocated buildings are in red. The x and y coordinates (m) define the horizontal domain extent in the west–east (x) and south–north (y) directions.

To investigate how the changes in the built environment affect the wind flow, different layout cases were generated by modifying the spatial arrangement of the buildings in the campus. For modifying the building configuration, several approaches were explored, including the random rearrangement of the buildings across predefined grid cells and the relocation of individual buildings of the campus area. Details on the initial methodological approaches that were explored, before adopting the final method, are provided in Appendix B. Although these methods produced a wide range of configurations, they proved impractical for the purpose of the study. Since the available space for moving the buildings within the domain is limited, the resulting layouts could not preserve the overall structure of the campus, including the road network, the central open space and the main building groups, and therefore they missed realism.
For these reasons, the chosen approach focuses on modifying the campus layout by manually moving buildings in groups. This strategy allows greater control over the modified layouts, ensuring that the overall character of the campus, such as its road network, open spaces and vegetation is preserved. Moreover, moving buildings in groups, instead of individual buildings, introduces larger modifications in the original campus layout with a limited number of alteration steps. These changes are more likely to generate observable variations in the wind field, which makes the effects of the different layouts easier to compare.

The changes in the layout were applied in the central part of the campus which represents a zone frequently used by pedestrians and cyclists. This area is therefore considered particularly important for assessing the impact of building arrangements on the wind flow.

All geometry modifications were carried out using Blender GIS. The original building geometry was imported in wavefront OBJ format and was edited to create the new layouts. For each case, the selected buildings were first grouped together and then transferred and rotated within the horizontal plane. After modification, the new geometries were exported again in OBJ format. For each modified layout, selected buildings were identified and grouped so that each building group was handled as a single object during the modification process.

The final layouts are presented in Figure 3.6, where buildings that were relocated are highlighted in red.

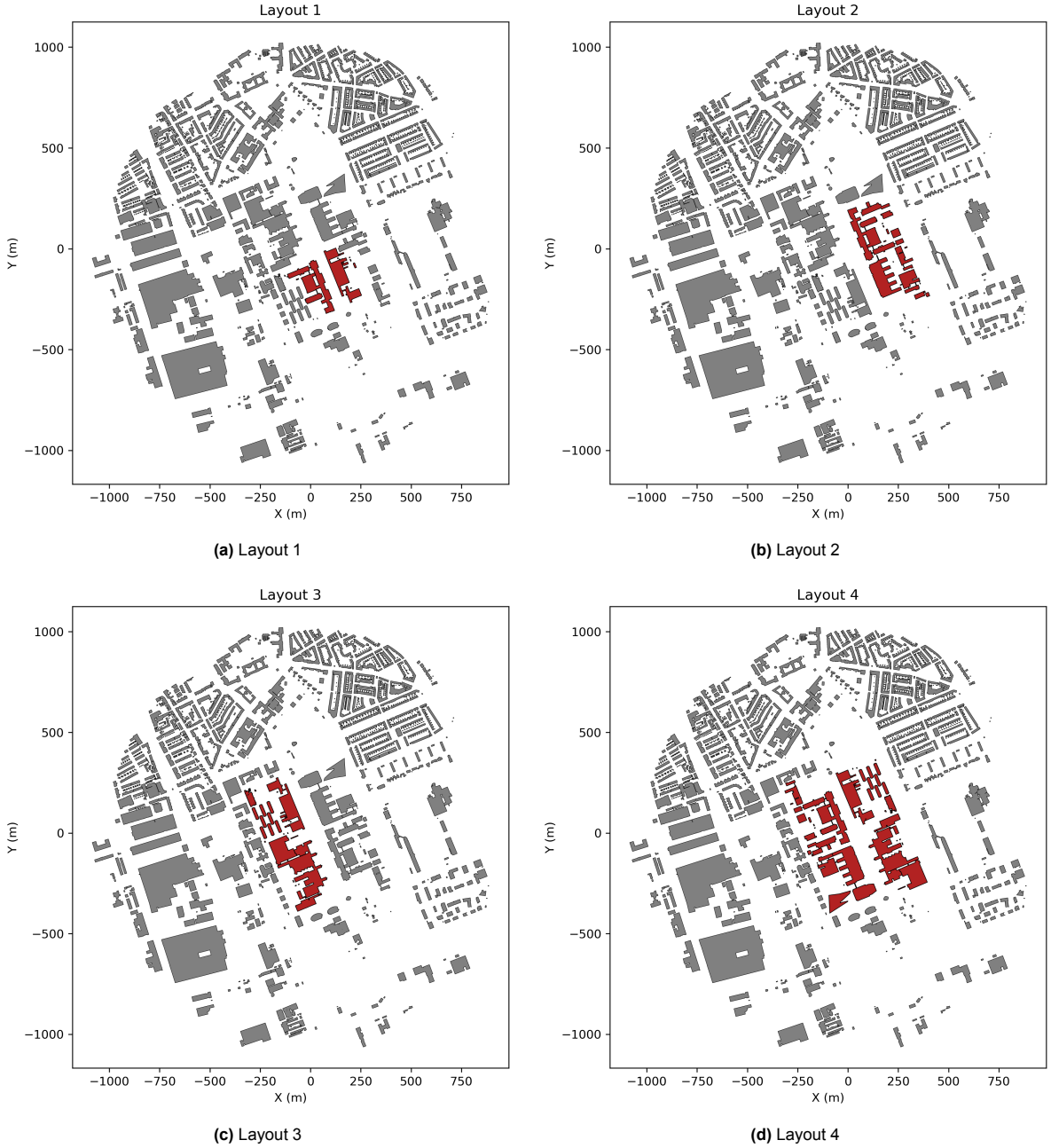

(a) Layout 1

(b) Layout 2

(c) Layout 3

(d) Layout 4

Figure 3.6: Modified campus layouts in plan view. Grey polygons represent the unchanged building footprints while relocated buildings are highlighted in red. The x and y coordinates (m) define the horizontal domain extent in the west–east (x) and south–north (y) directions.

3.2.4. Mesh generation

To enable the numerical simulations, we first defined the computational domain of the study area and then discretized it by generating a mesh, based on the geometries described above. The mesh generation was performed in open-source CFD software OpenFOAM, version 7 (OpenFOAM Foundation, 2021), using the `blockMesh` and `snappyHexMesh` utilities.

The `blockMesh` utility was used to define the computational domain, including its size and the resolution, and to generate the background mesh. The computational domain was defined as a cylindrical volume surrounding the building area. The cylindrical shape was chosen because it allows running the simu-

lation for multiple wind directions using the same computational mesh. The dimensions of the domain were selected based on the height of the tallest building in the study area ($H_{\max} \approx 96$ m), following the best-practice guidelines for urban flow simulations (Franke et al., 2007). According to this, the domain should ideally extend $15H_{\max}$ behind the buildings in the horizontal direction and $5H_{\max}$ in the vertical direction.

Based on these requirements, the dimensions of the computational domain are summarized in Table 3.2.

Table 3.2: Spatial extent of the computational domain.

Domain bound	Spatial extent (m)
$x_{\min}$	-3760
$x_{\max}$	3760
$y_{\min}$	-3760
$y_{\max}$	3760
$z_{\min}$	-5
$z_{\max}$	576

These dimensions allow the flow to develop to a steady background flow, undisturbed by the presence of buildings, ensuring that the boundary conditions do not influence the flow in the area of interest.

Figure 3.7: Top view of the computational domain. Buildings are modeled only within the inner circle (study area). The outer region contains no buildings and it is modeled as flat surface with different layers (terrain, vegetation and water). The different colours indicate: buildings (dark grey), vegetation (green), water bodies (blue), and terrain (light grey).

The computational domain was discretised using a hexahedral mesh. The inner region, that includes the buildings, was discretized using a finer resolution of 38×38 cells in the horizontal directions while for the area between the inner region and the outer boundary of the computational domain 27×27 cells were used. In the vertical direction the domain was divided in two regions, consisting of 5 cells near the ground and 7 cells in the upper region.

After generating the background mesh, the mesh was further refined using the `snappyHexMesh` utility. The mesh resolution was controlled using refinement at different levels, with higher refinement levels corresponding to finer resolution in the mesh. Two refinement regions were defined around the area of interest. The inner region that includes the buildings, was discretized using a higher refinement level, while the surrounding region was refined at a lower level. In addition, different refinement levels were applied based on distance from the buildings and surface geometries, resulting in higher mesh resolution near the surfaces and coarser resolution further away.

The two mesh refinement strategies adopted in this study are presented in Tables 3.3 and 3.4.

Table 3.3: Region-based mesh refinement applied to the background mesh.

Refinement region	Refinement level
Inner refinement region	2
Outer refinement region	1

Table 3.4: Distance-based mesh refinement applied to surface geometries.

Surface type	Refinement level	Maximum distance from surface
Buildings	5	$4\ \mathrm{m}$
	4	$12\ \mathrm{m}$
	3	$25\ \mathrm{m}$
Terrain	5	$3\ \mathrm{m}$
	4	$5\ \mathrm{m}$
Water	5	$3\ \mathrm{m}$
Vegetation	5	$3\ \mathrm{m}$

The choice of different refinement levels was made, because regions closer to the buildings and surfaces are characterized by stronger variations in the flow which need to be resolved at smaller scales.

Figure 3.8 provides an overview of the computational mesh.

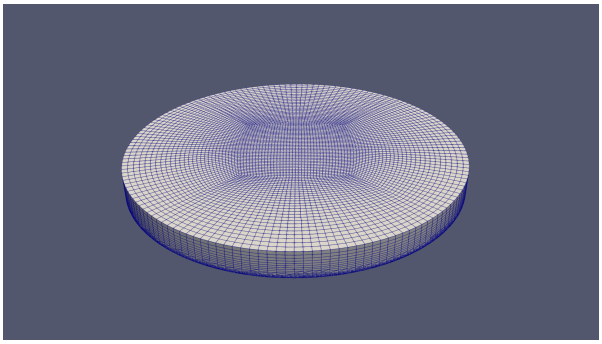

(a) Top view of the computational mesh.

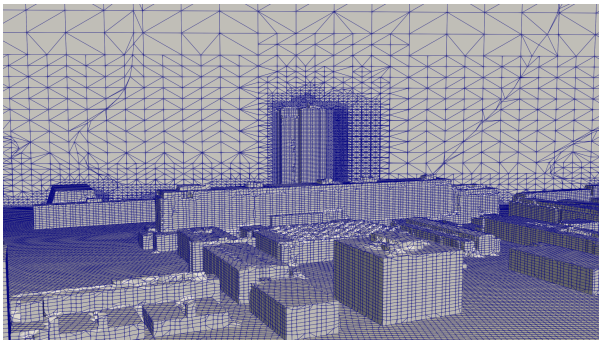

(b) Side view of the computational mesh.

Figure 3.8: Overview of the computational mesh used in the simulations, visualized in *ParaView.*

This procedure for the mesh generation was applied to the reference case and to all modified campus layouts using the same domain definition and refinement method. Before running the simulations,

for every case, the quality of the final mesh was verified using the OpenFOAM `checkMesh` utility and inspected in ParaView.

3.3. Simulation setup

After the generation of the computational mesh, the CFD simulations were carried out in *OpenFOAM*. In this section the setup and the execution of steady-state RANS simulations is described. All simulations were performed using the open-source CFD software OpenFOAM, version 7 on DelftBlue Supercomputer (Delft High Performance Computing Centre, 2024).

3.3.1. Flow modelling in OpenFoam

The flow in the domain was modelled as a steady, incompressible flow using the Reynolds-Averaged Navier–Stokes (RANS) approach. In this framework, only the time-averaged flow quantities are solved, while the effect of turbulence is modeled using closure techniques. It provides a statistical description of the flow and it is therefore suitable for studies of the wind flow in urban environments, where the primary interest is the mean wind field.

The governing continuity and momentum equations for incompressible RANS flow are given by Eqs. (2.6) and (2.7) in Chapter 2. In these equations, the Reynolds stress tensor introduces additional unknowns to the system of equations, leading to a closure problem. For the closure of the RANS equations, a turbulence model is required.

In the present case, the closure of the RANS equations is achieved using the standard two-equation k–ε turbulence model (Launder & Spalding, 1974), which is commonly used for wind flow simulations in the atmospheric boundary layer.

This model uses the Boussinesq eddy-viscosity hypothesis which computes the Reynolds stress tensor as the product of a turbulent eddy viscosity:

$$-\overline{u_i' u_j'} = \nu_t \left(\frac{\partial u_i}{\partial x_j} + \frac{\partial u_j}{\partial x_i} \right) - \frac{2}{3} k \delta_{ij}, \tag{3.1}$$

where k is the turbulent kinetic energy (TKE) and δ_{ij} the Kronecker delta.

The turbulent viscosity is computed as

$$\nu_t = C_\mu \frac{k^2}{\varepsilon}, \tag{3.2}$$

where ε denotes the turbulent kinetic energy dissipation rate and $C_\mu = 0.09$ is a model constant.

The transport equations for the TKE and the TKE dissipation rate ε are given by

$$u_j \frac{\partial k}{\partial x_j} = \frac{\partial}{\partial x_j} \left[\left(\nu + \frac{\nu_t}{\sigma_k} \right) \frac{\partial k}{\partial x_j} \right] + P_k - \varepsilon, \tag{3.3}$$

$$u_j \frac{\partial \varepsilon}{\partial x_j} = \frac{\partial}{\partial x_j} \left[\left(\nu + \frac{\nu_t}{\sigma_\varepsilon} \right) \frac{\partial \varepsilon}{\partial x_j} \right] + C_{\varepsilon 1} \frac{\varepsilon}{k} P_k - C_{\varepsilon 2} \frac{\varepsilon^2}{k}, \tag{3.4}$$

where P_k represents the production of turbulent kinetic energy and $\sigma_k = 1.0$, $\sigma_\varepsilon = 1.11$, $C_{\varepsilon 1} = 1.44$ and $C_{\varepsilon 2} = 1.92$.

3.3.2. Boundary conditions

The next step in the simulation setup is to determine the appropriate boundary conditions of the computational domain. The boundary conditions are applied to the different boundaries of the computational domain, corresponding to inlet and outlet boundaries, the top of the domain, and solid surfaces such

as terrain, buildings, vegetation and water bodies.

For the open boundaries, boundary conditions must be capable of reproducing a horizontally homogeneous atmospheric boundary layer under undisturbed conditions (Richards & Hoxey, 1993).

The vertical profiles for the mean wind velocity U, turbulent kinetic energy k and dissipation rate ε are defined as:

$$U(z) = \frac{u_*}{\kappa} \ln\left(\frac{z - z_g + z_0}{z_0}\right), \tag{3.5}$$

$$k(z) = \frac{u_*^2}{\sqrt{C_\mu}}, \tag{3.6}$$

$$\varepsilon(z) = \frac{u_*^3}{\kappa\,(z - z_g + z_0)}, \tag{3.7}$$

where u_* is the friction velocity, $\kappa = 0.41$ is the von Kármán constant, z_g is the displacement height, $z_0 = 0.5\ \mathrm{m}$ is the aerodynamic roughness length of the surface and $C_\mu = 0.09$ the constant of the k–ε turbulence model. The friction velocity u_* is calculated from Eq. (3.5) using a reference wind velocity $U_{\mathrm{ref}} = 5\ \mathrm{m\,s^{-1}}$ and a height of $z_{\mathrm{ref}} = 10\ \mathrm{m}$.

Here z_g is introduced as a vertical reference shift, because the geometry in the vertical coordinates includes negative values. Defining this height $z^* = z - z_g$ ensures that the logarithmic profile can be defined over the inlet boundary.To select an appropriate value for z_g, Eq. (**??**) is used. The equation contains the term $\ln(z - z_g + z_0)$, whose argument must be strictly positive in order for the logarithm to be defined. This requirement implies

$$z - z_g + z_0 > 0 \tag{3.8}$$

which gives:

$$z_g < z + z_0. \tag{3.9}$$

Furthermore, since the wind velocity must remain non-negative, the logarithmic term must satisfy:

$$\ln\left(\frac{z - z_g + z_0}{z_0}\right) \geq 0. \tag{3.10}$$

This condition is satisfied when

$$z - z_g + z_0 \geq z_0, \tag{3.11}$$

which leads to

$$z_g \leq z. \tag{3.12}$$

The most critical case for satisfying this condition is at the minimum vertical coordinate of the inlet boundary, $z_{\min} \approx -4.9$ m. As a modelling choice, z_g is defined slightly below this value by subtracting a small multiple of the roughness length. Using $z_0 = 0.5$ m, this results in

$$z_g \approx -5.4 \text{ m}.$$

All solid surfaces, including terrain, vegetation, water bodies, and buildings, were treated as no-slip walls. Wall functions were applied and different roughness lengths were assigned to terrain, vegetation, and water surfaces, while building surfaces were assumed to be aerodynamically smooth, meaning that standard smooth-wall functions were used.

Table 3.5 summarises the boundary conditions applied to each boundary of the computational domain.

Table 3.5: Summary of boundary conditions applied in the simulations.

Type	$\mathbf{U}$ (m s^{-1})	$\mathbf{p}$ (m^2 s^{-2})	$\mathbf{k}$ (m^2 s^{-2})	ε (m^2 s^{-3})	ν_t (m^2 s^{-1})
Inlet / Outlet	atmBoundaryLayerInletVelocity	freestreamPressure	atmBoundaryLayerInletK	atmBoundaryLayerInletEpsilon	calculated
Top	atmBoundaryLayerInletVelocity	freestreamPressure	atmBoundaryLayerInletK	atmBoundaryLayerInletEpsilon	calculated
Terrain	uniformFixedValue	zeroGradient	kqRWallFunction	epsilonz0WallFunction	nutkAtmRoughWallFunction
Buildings	uniformFixedValue	zeroGradient	kqRWallFunction	epsilonWallFunction	nutkWallFunction
Vegetation	uniformFixedValue	zeroGradient	kqRWallFunction	epsilonz0WallFunction	nutkAtmRoughWallFunction
Water	uniformFixedValue	zeroGradient	kqRWallFunction	epsilonz0WallFunction	nutkAtmRoughWallFunction

Selection of wind directions

For each layout the simulations were performed for 12 different inflow directions, which is considered sufficient for pedestrian wind comfort assessment studies (X. Chen et al., 2025; Franke, 2006). In order to ensure that these condition are representative of the prevailing wind conditions in the area of interest, the selection was based on an analysis of the local wind climate. Wind data were obtained from the Delfshaven weather station, accessed through the TU Delft weather database (https://weather.tudelft.nl/). This station was selected as it is the closest available station to the study area and provides a long-term wind dataset.

Results of the wind climate analysis are presented in Figure 3.9a and Figure 3.9b.

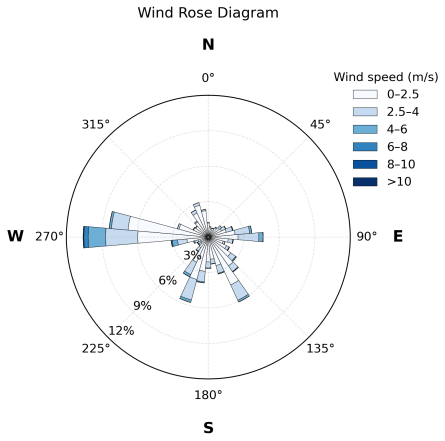

(a) Wind rose diagram for the Delfshaven weather station over the period 2015–2025.

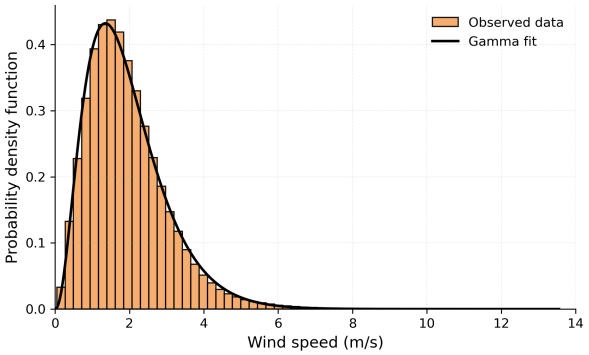

(b) Probability distribution of wind speed with fitted Gamma distribution.

As seen from the diagram, the most frequent wind direction is the west, with higher wind speeds observed from west and south-west. The probability density function of the wind speed is positively skewed, following a Gamma distribution.

To obtain a representative set of 12 wind directions, the Latin Hypercube Sampling (LHS) method was employed (Mckay et al., 1979). The wind directions selected follow the meteorological convention, in which the angle is measured clockwise from North. However, OpenFOAM defines the inflow wind

direction using a coordinate system with the reference direction in the West (0°) and angles increasing counterclockwise. Therefore, the meteorological wind directions had to be converted into the coordinate system used in the CFD simulations.
The list of the selected angles in meteorological convention, together with their corresponding converted angles used in the simulations are presented in Table 3.6.

Table 3.6: Selected wind directions (rounded): meteorological and converted angles.

Meteorological angle (°)	Angle (°) in OpenFOAM
257	13
209	61
193	77
162	108
147	123
112	158
87	183
44	226
344	286
299	331
282	348
274	356

3.3.3. Implementation

The simulations were performed for five layouts, for 12 different inflow wind directions in each, resulting in 60 simulations in total. All simulations were executed on DelftBlue Supercomputer (Delft High Performance Computing Centre, 2024).

The computational domain was decomposed for parallel execution, and each simulation was executed on 64 processor cores. The integral form of the governing equations were discretised using the finite volume method. Through the simulations, the mean velocity field U, pressure p, turbulent kinetic energy k, dissipation rate ε, and eddy viscosity ν_t were calculated for every cell of the mesh. These variables were computed by solving the steady-state RANS equations using the OpenFOAM solver `simpleFoam`, which resolves the equations through an iterative method, until convergence is achieved. The convergence was monitored by tracking the normalized residuals of the variables, as shown in Figure 3.10.

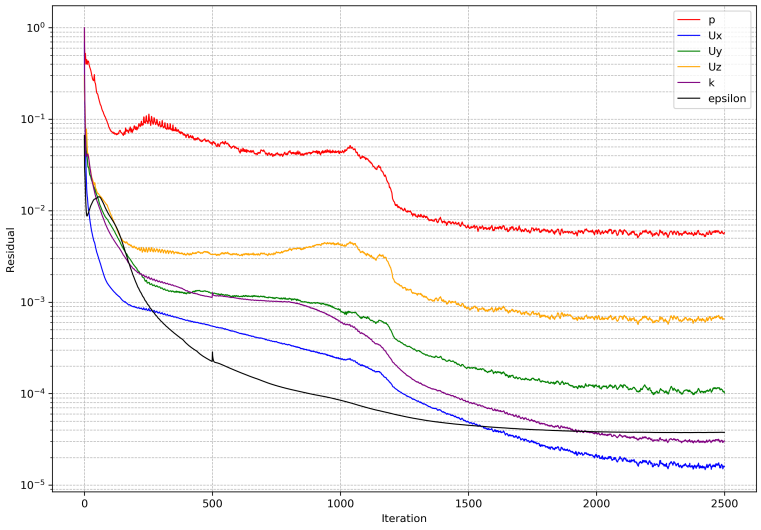

Figure 3.10: Residuals of pressure, velocity components, and turbulence quantities for a representative simulation case.

In order to improve the numerical stability of the simulations, values for the initial velocity were obtained using the solver `potentialFoam`. This solver computes a potential-flow solution and provides initial values that are closer to the expected flow field, making the simulation converge more smoothly during the early iterations.

In the initial phase of the simulations, a first-order scheme was applied to prevent instabilities during the early iterations, which was observed when second-order schemes were applied from the start. After 500 iterations, when the residuals started to stabilize, the scheme was switched from first-order to second-order to improve the accuracy of the solution.

Each simulation ran for 2500 iterations, until the residuals stabilized, indicating convergence of the solution.

3.4. Post-processing analysis

3.4.1. Contour plots

The simulated wind flow was analyzed at pedestrian level, at a height of $z = 2\ \mathrm{m}$. For each layout, in order to combine the effect of the selected inflow directions, the velocity magnitude was first computed for each wind direction at each point, as $|U_i|$ and then averaged over the selected wind directions as

$$U = \frac{1}{12} \sum_{i=1}^{12} |U_i|. \tag{3.13}$$

The velocity magnitude averaged over the wind angles was normalized by the inflow velocity at the boundary (U_{ref}) and contour plots of the velocity magnitude were generated.

To quantify changes in wind flow relative to the reference configuration, the difference in the averaged normalized velocity field was computed for each modified layout as

$$\Delta U = \frac{U_{\mathrm{mod,layout}}}{U_{\mathrm{ref}}} - \frac{U_{\mathrm{ref,layout}}}{U_{\mathrm{ref}}}. \tag{3.14}$$

where $U_{\mathrm{mod,layout}}$ and $U_{\mathrm{ref,layout}}$ are the averaged velocities of the modified layouts and the reference case. The difference was plotted for every layout.

For TKE, the same directional averaging and difference computation were performed and the was normalized by the inflow reference velocity scale, k/U_{ref}^2

$$\Delta k = \frac{k_{\mathrm{mod,layout}}}{U_{\mathrm{ref}}^2} - \frac{k_{\mathrm{ref,layout}}}{U_{\mathrm{ref}}^2}. \tag{3.15}$$

where $k_{\mathrm{mod,layout}}$ and $k_{\mathrm{ref,layout}}$ are the averaged TKE of the modified layouts and the reference case, respectively.

3.4.2. Wind comfort analysis

A pedestrian-level wind comfort analysis was performed to identify areas that experience uncomfortable wind conditions for pedestrians. The analysis was based on wind speed magnitude and TKE at a height of $z = 2\ \mathrm{m}$ above the ground.

Wind discomfort was assessed using exceedance criteria defined as fractions of the wind velocity U_{ref}. At every location, discomfort was assumed to happen when both of the following conditions were satisfied:

$$U > \alpha\, U_{\mathrm{ref}}, \tag{3.16}$$

$$k > \beta U_{\mathrm{ref}}^2, \tag{3.17}$$

where U is wind velocity magnitude and k the TKE and α and β dimensionless parameters. For each grid point, the fraction of wind directions for which the exceedance of both these conditions occurs was computed. This fraction was used as the probability of wind discomfort, with values ranging from 0, which indicates no exceedance for any wind direction, to 1, which means exceedance for all wind directions.

Similar to established pedestrian wind comfort criteria, the present method is based on threshold exceedance. However, whereas commonly used criteria are typically formulated in terms of mean or gust-equivalent wind speed, the present approach also includes TKE. Since TKE represents the intensity of velocity fluctuations around the mean flow, including it allows the assessment to account for the unsteady component of wind conditions that can contribute to the risk of unfavorable wind conditions for pedestrians. This method provides a consistent basis for comparing the discomfort risk across the different layouts, under the same set of representative inflow conditions. However, since the criterion requires both thresholds to be exceeded, it may not capture situations in which only one of the two quantities reaches elevated levels. In addition, although the relative sensitivity to wind velocity and TKE can be adjusted through the choice of α and β the resulting discomfort patterns remain dependent on the specific choice of these values.

In this study, the values $\alpha = 0.4$ and $\beta = 0.08$ were selected following the work of Patil and García-Sánchez, 2025. The resulting discomfort probability was visualized as contour plots for all the layouts.

3.4.3. Wind flow - Layout geometry relation

To further investigate the relation between the urban geometry of the layouts and wind flow, an additional analysis was performed focusing on a single inflow direction. The aim was to relate local wind velocity variations to the geometry of the different layouts.

Region of interest

For this, a representative region of interest (ROI) in the central open area of the campus was selected. The choice was made so that it remains open across all layouts. For this location, the direction corresponding to the highest wind velocity in the reference layout was identified. For this inflow direction, in each layout, the mean wind velocity was computed as the average wind speed over all grid cells within the region and then normalized using U_{ref}.

The circular ROI, defined within the central open area is shown in Figure 3.11.

Figure 3.11: Location of the circular region of interest within the central area of the TU Delft campus, defined as a red circle, used for the local wind velocity analysis.

The figure shows the ROI on the reference layout. The same area was applied to all modified layouts (see Results section 4.4).

Blockage ratios

Building blockage is a key factor affecting pedestrian-level wind flow, since buildings obstruct and redirect the approaching wind. As a result, different building arrangements are expected to modify the local wind conditions by changing the degree of blockage experienced by the flow. To quantify these geometric differences between the layouts and their effect on the flow, two metrics were calculated: the *frontal blockage ratio* and the *planar blockage ratio*. These metrics represent the amount of building surface exposed to the wind in the vertical plane and in the horizontal plane, respectively. Taken together, they allow to quantify how much of the incoming wind is blocked by the building arrangement, both vertically and horizontally. However, the local wind flow is also controlled by other mechanisms, such as wake formation and channelling. These blockage ratios should therefore be interpreted as geometric indicators that provide useful comparative information between layouts, rather than fully capturing the complexity of the local flow response.

To evaluate blockage consistently along the wind direction, the building geometry was rotated into a wind-aligned coordinate system (x', y'). The horizontal rotation aligns x' with the inflow direction and y' with the cross-wind direction.

The frontal blockage ratio shows how much of the flow is blocked by buildings when viewed in the vertical plane from a given wind direction. It can be defined as:

$$B_{\text{frontal}}(z) = \frac{L_{\text{blocked}}(z)}{L_{\text{domain}}(z)},$$

where $L_{\text{blocked}}(z)$ is the total width of the buildings intersecting the flow at height z, and $L_{\text{domain}}(z)$ is the total width of the domain at a specific height.

To compute this metric, the 3D building geometry was first rotated to the wind direction and then projected on the plane perpendicular to the flow ((y', z) plane).

To obtain a height blockage measure, horizontal slices of $1\ \text{m}$ thickness were placed at regular height intervals of $2\ \text{m}$. For each height level, the slices intersect with the projected buildings. The horizontal widths of buildings that intersect with the slice are summed to obtain the total blocked width at that height. This blocked length was then divided by the total cross–wind width of the domain. A visual representation is shown in Figure 3.12

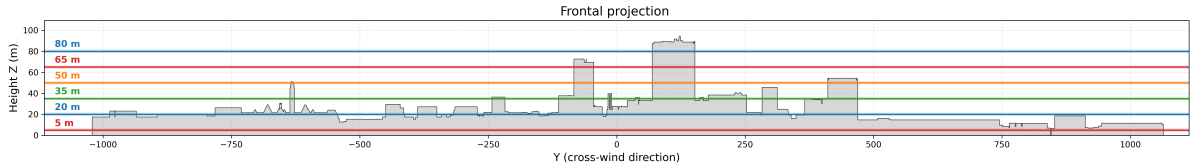

Figure 3.12: Frontal projection of the TU Delft campus buildings for a wind direction of 0° (from the west). The colored bands show the horizontal slices used to compute the frontal blockage ratio at different heights.

Since the frontal blockage profiles differ most clearly in the height range of 25–35 m, a representative frontal blockage metric was computed by averaging the frontal blockage ratio over this interval. This procedure was repeated for all layouts.

The planar blockage ratio shows the horizontal flow cross-section that is occupied by buildings and it is defined as:

$$B_{\text{planar}}(x) = \frac{A_{\text{blocked}}(x)}{A_{\text{domain}}(x)},$$

where $A_{\text{blocked}}(x)$ is the width of the domain occupied by buildings at the direction of the wind and $A_{\text{domain}}(x)$ is the total width of the domain at that location. Same as in frontal blockage ratio, after rotating the city geometry to align with the wind direction, vertical slices were then taken along the wind axis. A total of 200 slices were used, uniformly spaced along x', each of which had a thickness of $10\ \text{m}$. For each slice, the total blocked width was computed as the sum of all building intersections within the slice. Then it was divided by the total crosswind domain width, as shown in Figure 3.13

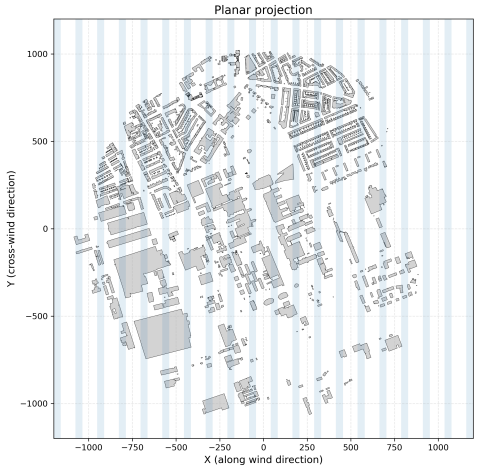

Figure 3.13: Top view of the TU Delft campus buildings for a wind direction of $0°$ (from the west). The colored bands represent the horizontal slices used to compute the planar blockage ratio at different locations.

Because the ROI is relatively small compared to the domain, the planar blockage ratio was computed locally around the area of interest. Instead of using the full cross-wind width of the domain, the calculation was restricted to a width of $w = 250m$ around the ROI.

A cross-wind corridor of width w was defined around the rotated ROI center $y'_c = -20$:

$$y' \in \left[y'_c - \frac{w}{2},\ y'_c + \frac{w}{2} \right].$$

To relate the blockage ratio geometry to the wind inside the ROI, the blockage ratios were extracted at the upstream boundary of the ROI and at the upstream area before the flow enters the ROI. The upstream entry location for a radius R is defined as:

$$x'_{\text{entry}} = x'_c - R,$$

where $x'_c = -25$ is the coordinate of the center of the ROI in the rotated system.

The upwind section of length $L = 50\ \text{m}$ was selected upstream of the entry point, extending from: $x'_{\text{entry}} - L$ to x'_{entry}, i.e.

$$x' \in \left[x'_{\text{entry}} - L_{\text{up}},\ x'_{\text{entry}} \right].$$

This value was chosen based on the findings of Reiter (2010), who reported that, for streets aligned with the wind the wind protection effect of the buildings diminishes over a distance of approximately $50\ \text{m}$ upstream of the area.

For this part the blockage ratios across the wind flow direction was computed and the mean upwind blockage was computed as the average blockage ratio over this area:

$$B_{\text{mean}} = \frac{1}{N} \sum_{i=1}^{N} B_i.$$

Same as with the frontal blockage ratio, the computation was repeated for all layouts.

A visualization of the local planar blockage-ratio is presented in Figure 3.14.

Figure 3.14: Visualization of the planar blockage-ratio in the reference layout. The figure shows the region of interest (ROI), the entry location x'_{entry}, the cross-wind corridor of width w, and the upstream section of length L used to compute the mean planar blockage ratio. The geometric quantities are defined in the rotated wind-aligned coordinate system (x', y').

The same visualizations for the modified layouts are included in Appendix section A.7.

4

Results

This chapter presents the results of the CFD simulations and the analysis performed, including the averaged wind field and the TKE at pedestrian height, wind comfort analysis and the relation between the local wind variations in each layout and the blockage ratios.

4.1. Wind field at pedestrian level

The wind field averaged over all directions at pedestrian level ($z = 2\ \mathrm{m}$) is shown in Figures 4.1 and 4.2, for the reference configuration and the modified layouts, respectively. The results are presented in terms of the normalized mean wind velocity, U/U_{ref}, in order to facilitate comparison between the different configurations.

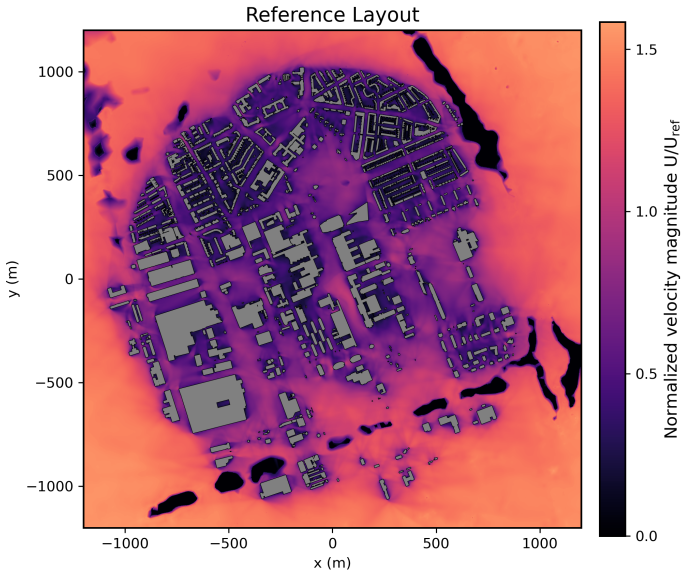

Figure 4.1: Directionally averaged normalised wind velocity at pedestrian level ($z = 2\ \mathrm{m}$) for the reference layout.

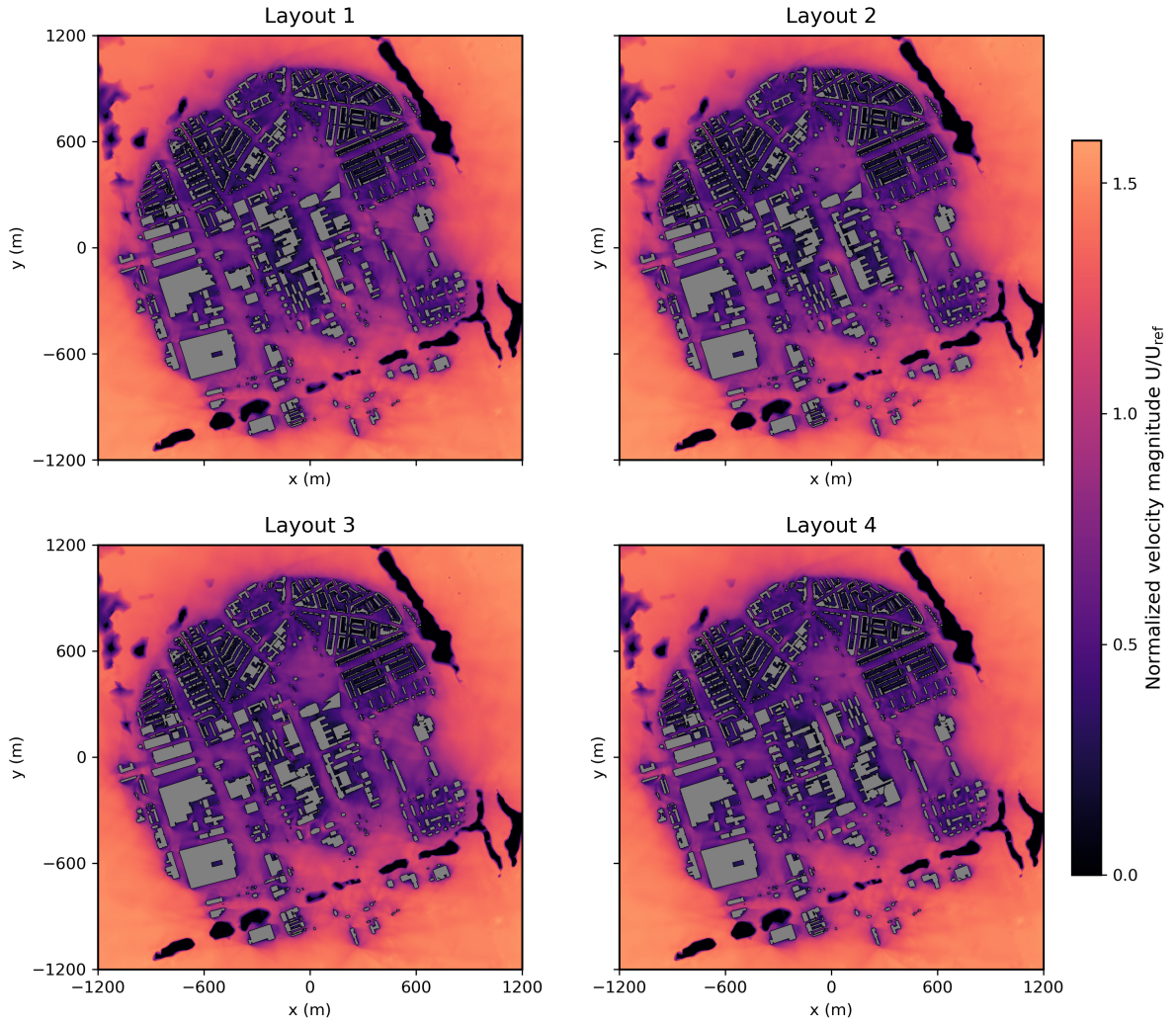

Figure 4.2: Directionally averaged normalized wind velocity at pedestrian level ($z = 2$ m) for the modified layouts.

For all layouts, the averaged wind velocity at pedestrian height shows that variations in mean wind velocities occur mainly in the central area of the campus. In this area, the local wind velocity reaches values between 1 to 1.5 times the inflow reference velocity. Lower wind speeds are observed close to the buildings and areas with near-zero averaged velocities appear mainly in sheltered areas between the buildings. To make these local changes in the main central area easier to distinguish, zoomed-in views are provided in Appendix section A.2.

Although the overall patterns seem quite similar across the different layouts, especially in the open areas away from the buildings, local variations can be observed. To compare the changes in wind velocity between the reference configuration and the modified layouts, the difference between the averaged normalized velocity of the layout and the reference configuration was also plotted. Results are shown in Figure 4.3.

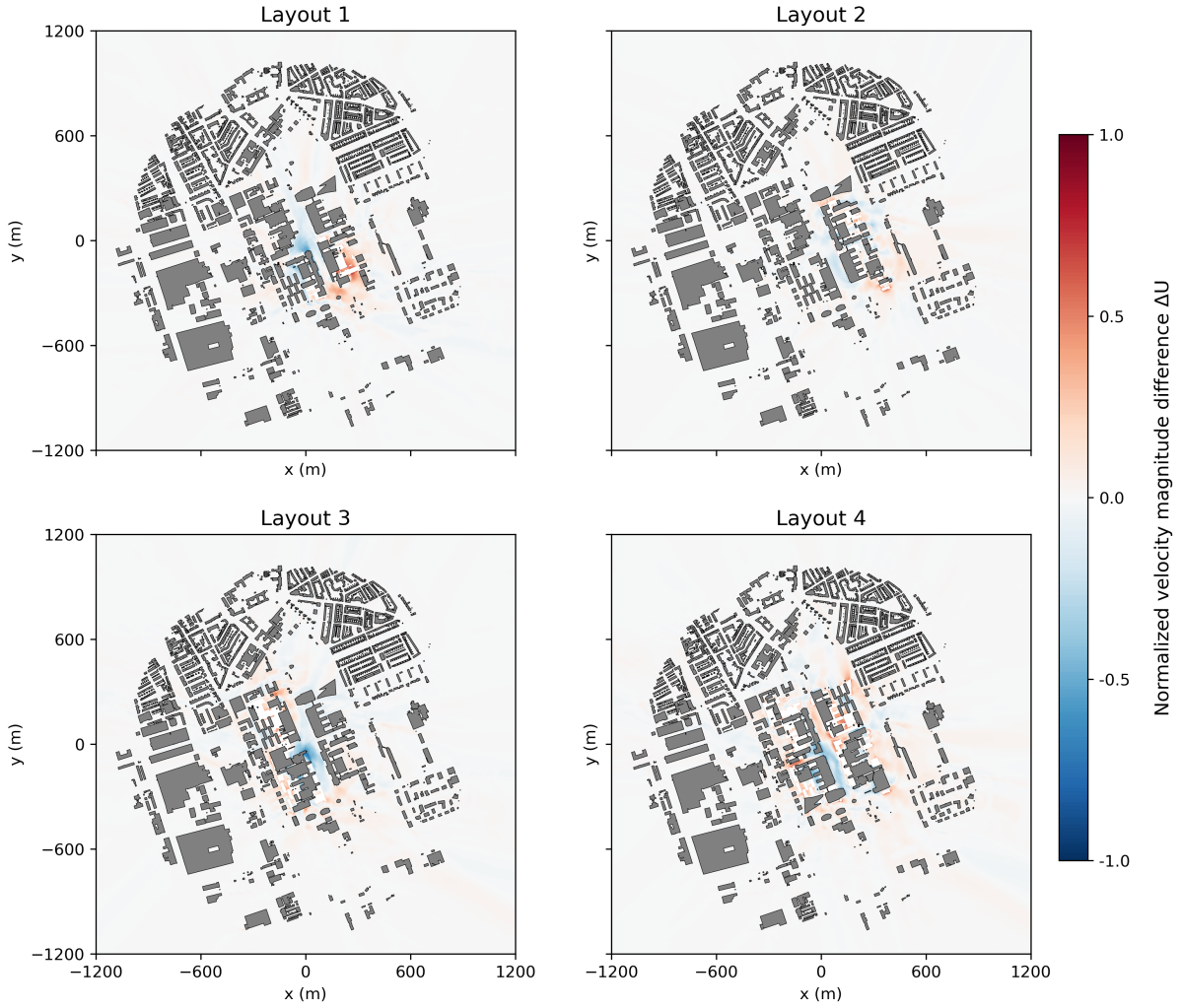

Figure 4.3: Difference in wind velocity magnitude at z = 2 m, averaged over 12 angles for the four modified layouts. Blue color indicates decrease in the wind velocity and red color increase.

Across all modified layouts, the largest deviations from the reference case occur in the main part of the campus, from north-west to south-east direction. These changes (either positive or negative) are mainly observed in regions close to the buildings which moved. Each modified layout shows different local variations in the wind speed.

In Layout 1, the biggest difference is observed around the EEMCS building which was repositioned in the place of CEG, where the wind speed increases. On the other hand, a small decrease in velocity appears close to the new location of CEG building, extending also in the northern part of the campus. This pattern can be explained as a result of the relocation of the EEMCS building. In the reference configuration, the tall EEMCS tower redirects flow from higher elevation towards the ground through downwash, creating zones of wind acceleration around it. After relocation, this downwash effect is transferred to the new tower position, which can explain the local increase there, mainly in the south part of the relocated EEMCS tower. The new layout also modifies the exposure of the streets and open spaces. Since the most dominant inflow wind in the simulation corresponds to westerly directions, the building arrangement of Layout 1 provides greater shielding for specific parts of the campus. This is reflected in the main central open area, between the ME and AP buildings. In the reference setting the presence of the EEMCS building affects the flow reaching the central open space, leading to higher wind speeds in that area. After relocating the tower, this downwash is not present anymore and as a result, lower wind speeds are observed in these regions.

Layout 2 shows the smallest changes of all layouts. According to Figure 4.3, the variations in wind ve-

locity are less pronounced and concentrated in the east part of the campus where the change between the buildings of CEG and AP faculty took place. A strong increase in the magnitude can be observed around the new location of the SW2 in the south part of the area, as a result of higher exposure of the tall building to the flow, compared to its previous position. Moreover, a localized zone of increased wind speed appears in the passage between the relocated CEG building and the AULA. This can be attributed to the modified permeability of the built layout: compared to the reference configuration, the rearrangement reduces the available flow passages between the AP and CEG buildings, since the two buildings in this layout are very close together and the street corridor between them is practically eliminated. Therefore, more of the approaching flow is forced through the remaining opening that connects the central open area to the eastern areas of the campus, leading to stronger winds in this corridor (funnelling effect). A small decrease in wind speed is also observed near the relocated AP building. This change is associated to the replacement of the CEG with the shorter AP building. For westerly inflow, the upwind EEMCS tower drives downwash and increases the velocity near the ground. In the reference layout, the taller CEG building downwind can further increase this local speed-up through additional blockage. As a result, replacing it with a shorter building reduces this interaction and decreases the wind velocity, as more airflow can pass over the rooftop rather than being forced around the building at pedestrian level. For easterly inflow, the CEG building at this location produces stronger facade downwash, whereas AP tends to weaken these effects, due to its smaller size.

Layout 3 shows stronger local variations. Most changes in velocity magnitude are observed in the west part of the campus, where the EEMCS and ME buildings were swapped. Around the new position of the EEMCS building the wind speed increases, as the building is now in a more exposed area. The highest increase occurs in the north part of the building on the northern side of the building, which faces the north–easterly inflow more directly. On the other hand, around the new location of ME the velocity experiences a large decrease of $1\ \mathrm{m/s}$, compared to the reference. However, this decrease is not concentrated only around the relocated ME, but also in the main open space area. This can be attributed to two combined effects. First, same as discussed before for Layout 1, replacing the EEMCS tower with a lower building reduces the wind acceleration near the ground, as the flow experiences less induced downwash and as a result less flow is redirected. In addition the new arrangement seems to slightly increase the space between the ME and CEG buildings, making this area more open. Compared to the reference case, the corridor is less narrow and as a result weakens flow channelling and leads to lower wind speeds locally. Finally a new low speed region is formed between the EEMCS and ME buildings. This is in line with the sheltered area that is created between the buildings where the flow is blocked from all wind directions. Due to the relatively low building heights of these buildings , no strong downwash is created in this region and as a result, the wind velocity remains low.

Layout 4 shows the largest increase in the wind velocity, among all the layouts, both in terms of magnitude and spatial extent. Localized increases in the wind are observed in the surroundings of the campus, mainly in the northern part. This can be explained by the fact that Layout 4 has the most building rearrangements. Similarly to the rearrangements in Layouts 1 and 3, the key driver is the movement of the EEMCS tower. Here, this effect is most pronounced on the side facing North, which is more exposed to the wind. In addition, this layout shows increased velocities between the buildings. Clear examples of this are the streets between the relocated CEG and AP buildings, where the reduced spacing forms a very narrow corridor opening, as well as the southern side of AULA and Library. This is expected since when the inflow direction aligns with these passages, the flow is funneled and accelerates locally. Finally, another noticeable feature in this layout is the contrast that the wind magnitude creates in the open space between the buildings. Here, results show increased wind speeds in the northern part but decreased wind speeds in the southern part. A possible explanation for this asymetry is the staggered placement of the EEMCS building relative to the main corridor alignment. As seen in Figure 4.3, the EEMCS is positioned slightly outside the corridor line in the northern sector. For the more frequent inflow directions, coming from the west and south sectors, the approaching flow encounters this exposed offset as a local obstacle along the corridor edge, it is deflected and guided along the main open space. As a result the wind experiences an increase of approximately $0.5\ \mathrm{m/s}$. This effect diminishes towards the southern part, where the region remains more sheltered and the wind velocity is reduced by up to $0.4 - 0.5\ \mathrm{m/s}$ relative to the reference case.

Overall, across the modified layouts, the velocity differences can be interpreted through the main flow effects that buildings have on the urban flow.

1. Tall buildings downwash (EEMCS tower and SW2):
   The EEMCS tower and SW2 building are the tallest structures of the domain and therefore, they produce strong downwash which transports higher momentum flow towards the ground. As expected, this increases pedestrian-level wind speeds near the base and also in downstream open areas. For EEMCS, this mechanism is noticeable in the layouts where the tower was relocated (Layouts 1, 2 and 4): the zones of increased wind speed are observed around the new position, while the magnitude of wind speed decreases in regions that were previously affected in the reference configuration. In the case of SW2, the relocation in Layout 1 also results in higher wind velocities around the region, especially in the southern part which is more exposed. This is consistent with the the tall building effects in pedestrian wind studies (Adamek et al., 2017; Stathopoulos & Wu, 1995).
2. Channelling:
   When the rearrangement reduces the space between buildings, the flow may accelerate locally through narrower passages, leading to increased velocity, as reported in previous studies (Mittal et al., 2018). A characteristic example of this is observed in Layout 2, where the modified configuration leads to an increase of velocity in the street between relocated CEG and AULA. A similar effect is observed in Layout 4, where a narrow passage forms between the CEG and AP buildings, resulting in increased velocities when the inflow aligns with this opening.
3. Sheltering:
   Several modified layouts exhibit a decrease in wind at pedestrian level relative to the reference case. The regions where this occurs often coincide with regions that become less exposed after the rearrangement. In Layout 1, visible changes, that can be attributed to the enhanced blocking of CEG, occur in the central open area. A similar sheltering response appears in Layout 3, where a new low-speed in the area of decreased speed forms between EEMCS and ME.
4. Near-building corner acceleration:
   Moving the building changes also the locations of acceleration near the buildings. According to the results, in all layouts high wind speeds remain concentrated close to the building edges. Areas that were previously more open or occupied by lower rise buildings, experience increased wind, once a higher building is placed nearby. This is the case in every relocation that involves the EEMCS and SW2, but also CEG in Layout 2.

4.2. Turbulence Kinetic Energy

The TKE at pedestrian level ($z = 2\ \mathrm{m}$), averaged over the selected wind directions was also calculated and visualized through color maps. Figure 4.4 corresponds to the reference layout and Figure 4.5 to the modified cases.

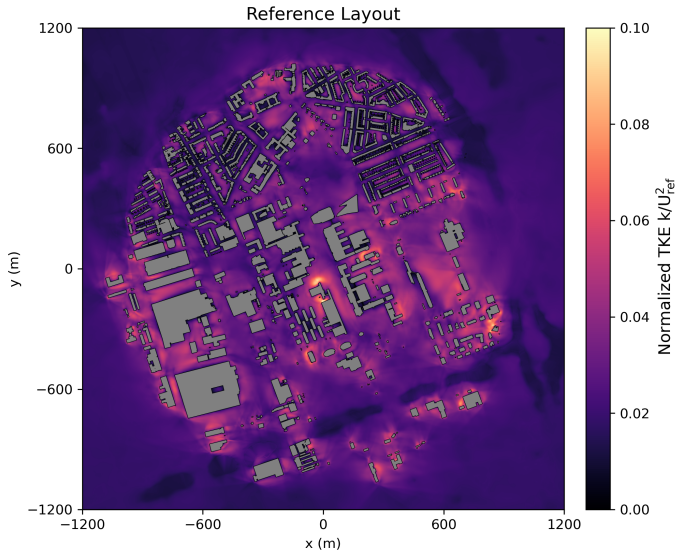

Figure 4.4: Directionally averaged normalized TKE at pedestrian level (z = 2 m) for the reference layout.

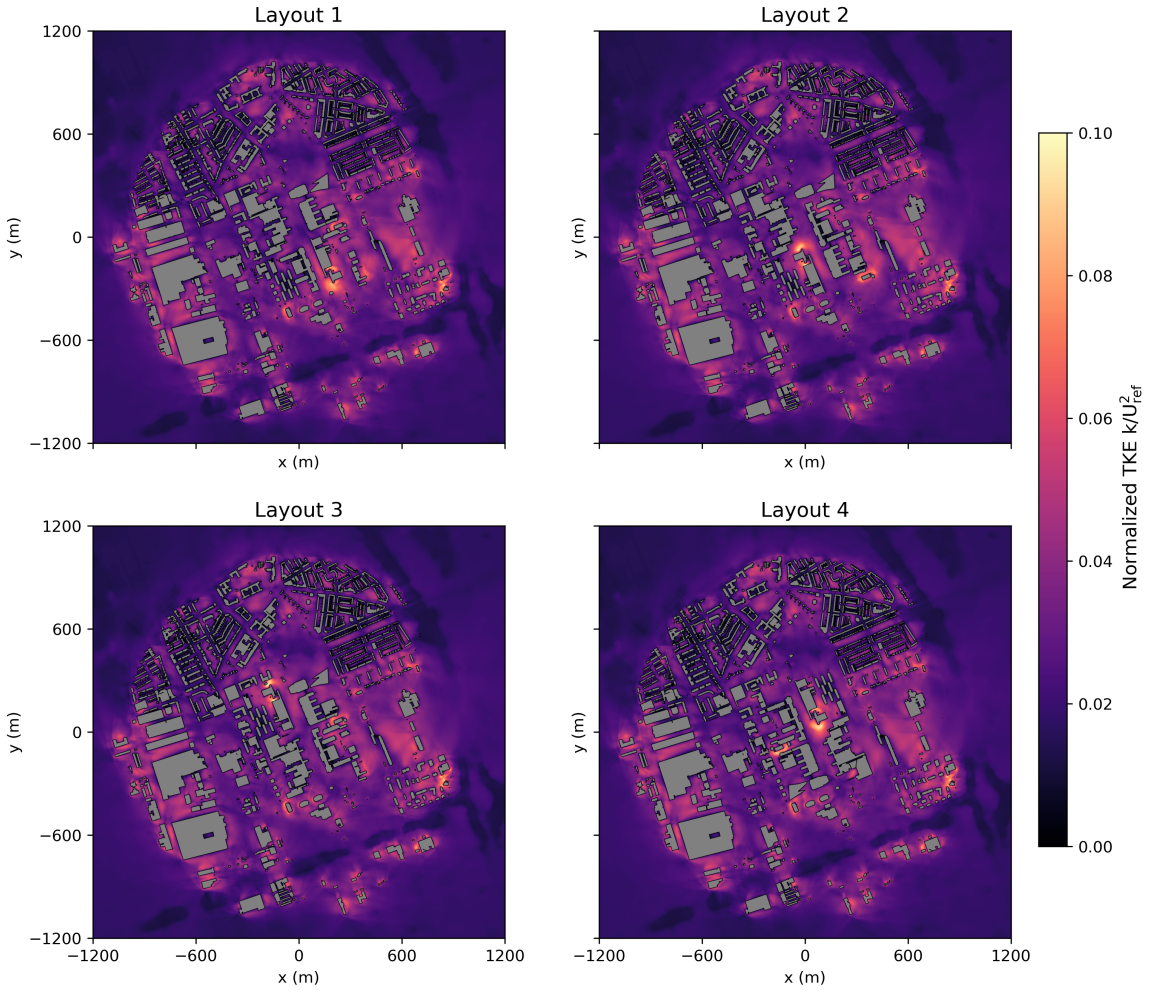

Figure 4.5: Directionally averaged normalized TKE at pedestrian level (z = 2 m) for the modified layouts.

In the reference layout, higher TKE values primarily occur near building edges and corners, where strong turbulence occurs. In contrast, lower values are visible in open spaces, where flow is more uniform. The modified layouts exhibit similar overall TKE patterns. However, the distribution of these areas is different between layouts, due to different building arrangement.

The difference in TKE between the modified layouts and the reference layout is calculated, as shown in Figure 4.6.

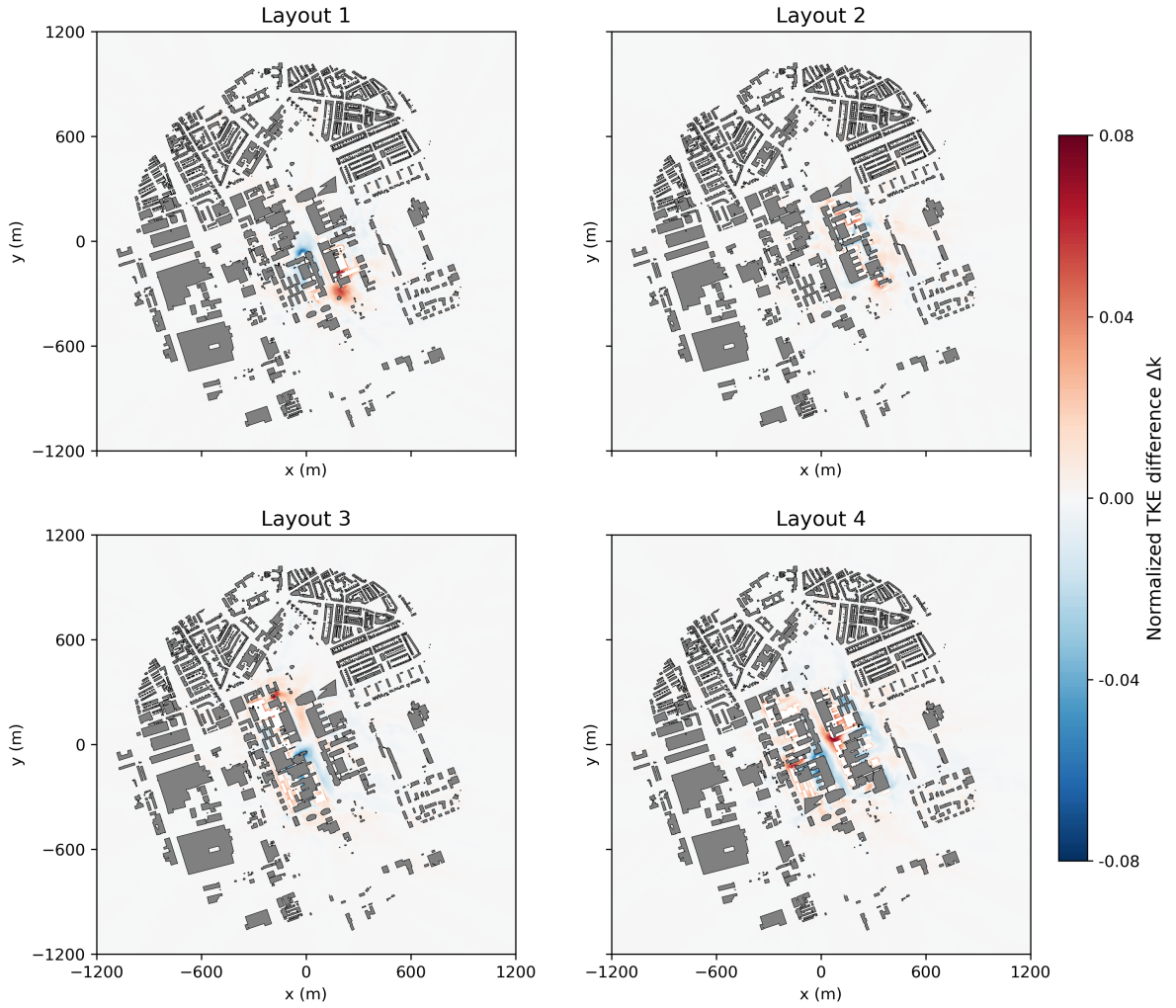

Figure 4.6: Difference in TKE at z = 2 m, averaged over 12 angles for the four modified layouts.Blue color indicates decrease in the wind velocity and red color increase.

Changes in TKE are highly localized and mainly observed near the regions where geometric modifications took place. Away from the relocated buildings the variation of TKE is close to zero, indicating that the rearrangement mainly redistributes turbulence locally, following the new locations of buildings.

Layout 1 exhibits changes in turbulence intensity, in the regions around the EEMCS and CEG buildings, that were relocated. An increase is observed around the relocated EEMCS tower, which indicates that the turbulence zone has shifted with the tower position. The zone of high TKE presents larger spread compared to the reference case. On the other hand, at the previous tower location, TKE decreases, as the strong downwash created by the tall tower has been removed in that area.

In Layout 2 the changes are much smaller, with most variations observed in the east side of the campus around the moved buildings. A clear zone of increased TKE appears around the relocated SW2 building in the southern part of the domain, which is again consistent with the tall building in this location. Outside

the modified building group, TKE difference remains small.

Layout 3 shows more pronounced differences from the reference, particularly around the buildings on the west side. The high-turbulence zone follows the displacement of the EEMCS building, as expected, while around the ME area TKE decreases, as the much lower building produces less turbulent flow. The high TKE spot around the tower remains more limited around the building. Small changes can also be observed in the open space in the center of the campus, with a decrease in front of relocated ME and increase around EEMCS.

Layout 4 exhibits the largest changes in turbulence. While the variations remain related to the relative positions of the buildings, here the regions where TKE has changed extend over a larger area. This can be again attributed to the fact that this layout experiences the largest modifications. Increased TKE appears in the corner of EEMCS tower and behind it. In the old location of the tower, where AP has moved, TKE has decreased, reflecting the weaker turbulence produced in this location after the modification. Additional increase is also present around the new location of SW2 high rise building.

The results confirm that TKE at pedestrian height is mainly controlled by the campus geometry. Regions of increased TKE occur near the tall structures, such as EEMCS tower and SW2 where flow separation increases turbulence at pedestrian height (ASHRAE, 2005). This happens mainly around the corners, where corner acceleration is known to occur (Reiter, 2010). As a result, replacing a tall building with a lower one reduces the turbulence at this location, as the TKE zone always follows the new location of the building. However around the relocated building the spatial extent of TKE tends to be different depending on the surrounding layout. More specifically, focusing on the EEMCS tower, the TKE increase is more concentrated when the tower is moved in the place of ME location (Layout 3) than when it is relocated to place of CEG (Layout 1) or AP (Layout 4). This can be attributed to the fact that in ME location, the tower is more sheltered and only exposed to the northerly inflow directions. This is n contrast to Layouts 1 and 4, where the tower is more directly exposed to a wider range of wind directions. A similar behavior is observed for SW2. In Layout 2, the relocation of SW2 in the southern part of the area creates a larger distinct zone of high TKE around the building. This is consistent with the absence of surrounding buildings which makes the building more exposed to the approaching flow and stronger velocities lead to higher turbulence levels. In Layout 4, the increase around the relocated SW2 is even more pronounced, since the new placement also increases the exposure of the building to the south-west inflow. These results agree with previous studies that show the effect of high-rise buildings on the pedestrian wind (Adamek et al., 2017; Blocken et al., 2012).

4.3. Pedestrian wind comfort assessment

The following figures present the probability of discomfort for the reference and modified layouts at pedestrian height. They were computed by evaluating the exceedance of a combined velocity and turbulence thresholds for each of the 12 simulated inflow directions. As described in Chapter 3, the the parameters α and β are not standardized, which means that different choices result in different probabilities. Different combinations can be found in Appendix section A.4. The following plots correspond to $\alpha = 0.4$ and $\beta = 0.08$

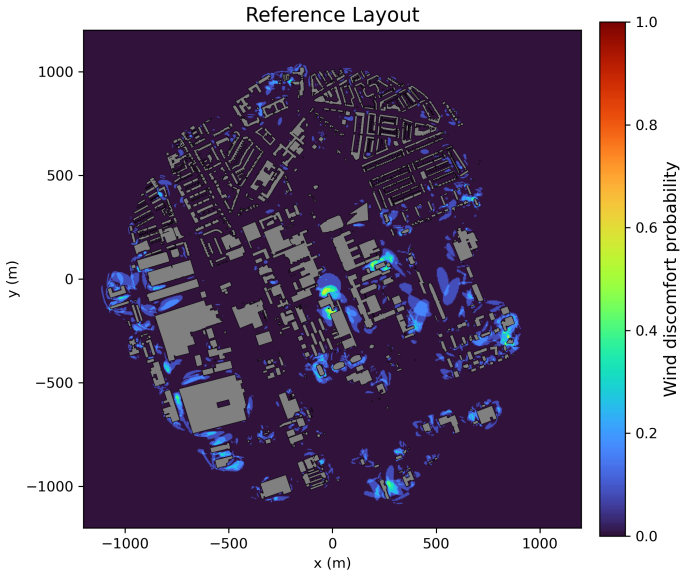

Figure 4.7: Wind comfort map at pedestrian level ($z = 2$ m) for the reference layout.

In the reference layout, the highest discomfort probabilities are concentrated around the EEMCS tower. Values reach approximately 0.6-0.7 on the northern side and behind the building, while probabilities of about 0.2-0.3 extend in the open space on the front side. Lower discomfort probabilities also appear in the open area between EEMCS and CEG, indicating the impact of the tall building in the surrounding area. A second notable discomfort location is observed on the north side of SW2 building, with a probability of approximately 0.5. These locations agree with previous wind comfort studies on the campus (Patil & García-Sánchez, 2025).

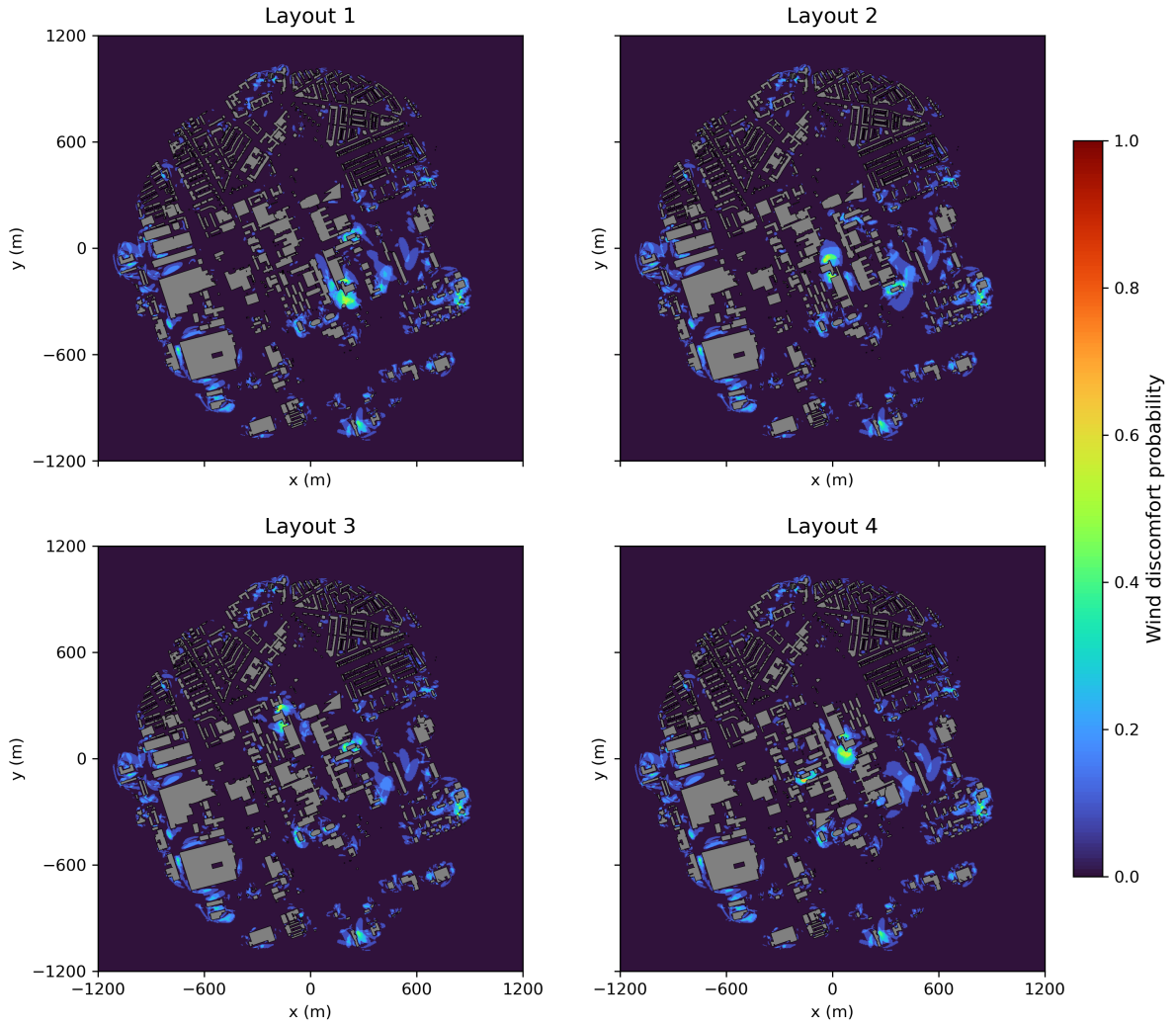

Figure 4.8: Wind comfort map at pedestrian level ($z = 2$ m) for the modified layouts.

For all layouts, the spatial pattern of the discomfort probability map is similar to the TKE distribution. This is expected, because the locations that generate high turbulence, such as edges of tall buildings and narrow passages, also experience high wind velocity, as seen from Figures 4.2 and 4.5. As a result, exceedance of the velocity threshold often coincides with increased TKE. However, the opposite is not necessarily true: high wind speeds that can also occur away from the buildings experience low turbulence that does not exceed the threshold and as a result they do not create pedestrian discomfort. Similar to the velocity and TKE results, the discomfort maps show clear differences between the modified layouts and the reference configuration, both in terms of the magnitude of the discomfort probability and the spatial distribution of the risk locations. These differences are mainly found in the central space of the campus, following the relocation of the buildings.

For Layout 1, the discomfort zone shifts together with the EEMCS building. Compared to the reference case, the intensity of discomfort appears similar, but it is spread in a larger area around the building. As a result, the main corridor also shows wider extent in the discomfort probability of approximately 0.2. The large spatial extent of the discomfort zone can be explained by the new location of the building, which is much more exposed compared the the reference, since there are no buildings on the southern side. This allows high-speed flow to be redirected from higher altitudes toward the ground, increasing the pedestrian-level wind. In addition to the main discomfort area around EEMCS, another discomfort zone appears on the eastern side of the smaller building next to it. Even though this area is also present in the reference layout, the probability is slightly higher in Layout 1. This is likely a direct consequence

of the EEMCS relocation. This pattern is primarily influenced by the west, south-west inflow direction, for which the EEMCS tower acts as an obstacle to the incoming flow. For this direction the tower induces downwash and transfers higher momentum wind to lower heights on the downwind side. A part of this accelerated flow passes above the roof of the adjacent lower building increasing its velocity. As the flow accelerates over the low roof it separates and forms a recirculation zone in the downwind side, which increases the turbulence near the ground, causing discomfort in the pedestrian level.

Layout 2 exhibits small changes compared to the reference case. The main discomfort region remains concentrated around the tower, since its position is unchanged in this configuration. Very small changes are visible in the main open space, which can be linked to the relocation of AP into the CEG position, however, the discomfort probability remains similar. The most noticeable difference occur near the southern side of the relocated AP building, as expected. A new discomfort zone is created around the SW2, with discomfort probability reaching approximately 0.5 there. This is consistent with the influence of the tall structure to pedestrian wind conditions. The only difference is that in the current layout this location extends further on the southern part of the building. This can be attributed to the increased exposure of the building in this layout, as there are no buildings to provide shielding from that side.

Layout 3 exhibits the largest reduction in wind discomfort areas in all modified layouts. The results show that the relocation of the EEMCS building leads to a weaker and more limited discomfort zone around the building. The largest reduction is observed in the northern side of the building, in which the discomfort probability has a value of 0.6 and does not extend in the front area of the building as before. This is expected as in the new configuration the tower is more protected from the strong inflow mainly from the south, due to the ME building. The remaining exposure is from the north side which corresponds to less dominant winds. Another contributing factor to the reduce of the discomfort are could be the fact EEMCS is closer to the neighboring buildings in the north and therefore this can limit the spatial development of the accelerated flow which in turn restricts the discomfort area. Apart from that, only a small region of low probability appears near the neighboring building in front of the AULA. In the rest of the open space area the pedestrian wind conditions have significantly improved, exhibiting very low, near zero discomfort. Regarding the eastern part of the campus, no changes are observed, since the local layout remained unchanged.

In Layout 4 the wind discomfort region again follows the new location of the EEMCS. Compared to the reference case, the affected area is more extensive around the building edges. This is partly expected due to the tower height, however the increased extent suggests that the surrounding layout also affects the wind flow near the ground. A likely contributing factor is the placement of CEG on the west side. For westerly winds, the wake region behind CEG is reinforced by downwash in the windward face of EEMCS, leading to turbulent flow and worse pedestrian conditions in the open space between the two buildings. On the other hand, the south part of the main open corridor presents no discomfort risk. In this sense, the rearrangement in Layout 4 appears to redistribute the discomfort regions: conditions improve in the southern section, while the risk becomes higher in the upper part.

In summary, the results show that building rearrangement can significantly affect the spatial distribution and the intensity of pedestrian wind discomfort across the campus. Across all modified layouts, the primary discomfort locations consistently follow the relocation of the tallest buildings (EEMCS tower and SW2), indicating that high-rise placement is the major key driver of the pedestrian wind condition. This is consistent with the established literature, which shows that tall buildings tend to increase winds in pedestrian-level through mechanisms such as downwash and enhanced turbulence near building corners (Adamek et al., 2017; Blocken et al., 2012; Zhang et al., 2020). While the main discomfort locations move together with the the tall buildings new positions, the spatial patterns are not the same across layouts. When a tall building is moved to a more exposed location with respect to the strongest prevailing wind (south-westerly sectors), the discomfort region tends to extend over a larger area around the buildings. On the other hand increased shielding by nearby buildings can limit the development of accelerated flow and improve the pedestrian-level wind conditions. In addition, the orientation of the relocated building relative to dominant wind directions has a further impact on this effect, as stated

by Reiter (2010). More specifically, relocation of the high-rise buildings to the direction with less wind (north sector in this study) is associated with a more confined affected area of discomfort. However, since the relocation changes both the surrounding configuration and the building's exposure to different inflow directions at the same time, it is not possible to isolate each effect and quantify its magnitude. Finally, the results indicate that relocation affects are not always restricted around the moved building. In several layouts, the modified high buildings locations alters wind conditions in adjacent open spaces and downstream regions, by interacting with neighboring buildings, which is in line with previous studies (ASHRAE, 2005). In particular, placing a tall building upwind of a lower structure can produce elevated discomfort on the leeward side of the lower building. From a design layout perspective, these findings also align with prior guidance that increasing open spaces by removing high obstacles can improve pedestrian wind comfort by limiting local accelerations (Mittal et al., 2018).

Comparing the modified layouts, Layout 2 and 4 mainly redistribute the discomfort, but they do not show clear overall improvement or worsening compared to the reference case. Layout 1 leads to worse pedestrian conditions overall, as the discomfort risk is spread over a larger area. Finally, Layout 3 shows an improvement, with discomfort region becoming more restricted in the main campus area.

4.4. Influence of blockage ratio on wind flow

To examine the directional variability of the wind flow at pedestrian level, the velocity magnitude fields were plotted for all wind directions selected in the simulation. An animated visualization of the pedestrian-level wind velocity fields for all simulated wind directions is provided and can be accessed via the QR code included in section A.3 of the Appendix.

Among all the wind directions, the case corresponding to a wind direction of 147° was found to produce the highest wind velocities in the central corridors of the campus. These open spaces are typically characterized by high pedestrian activity and are therefore considered relevant from a wind comfort perspective.

As a result, the 147° wind direction was selected for further analysis.

The color maps of the velocity magnitude for this wind direction is shown in Figure 4.9, while for the rest layouts can be found in Appendix section A.5

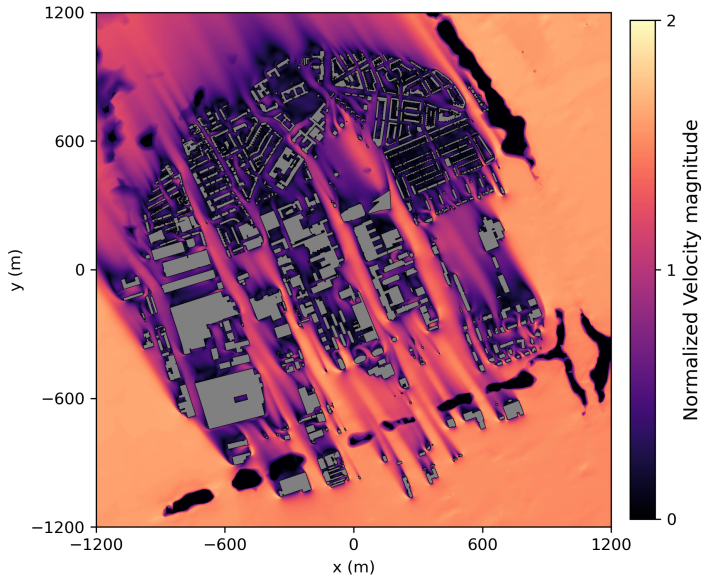

Figure 4.9: Wind velocity magnitude at pedestrian level ($z = 2$ m) for the 147° wind direction.

The circular region of interest, defined within the central open area is shown in Figure 4.10.

Figure 4.10: Location of the circular region of interest (ROI) for the reference and modified campus layouts. The ROI is shown as a red circle and was used for the local wind velocity analysis.

For each layout, the mean wind velocity was calculated, by averaging the velocity magnitudes of all grid points inside the circular region. The calculations were made for a radius of 5, 10, 15, and 20 m in

the circular region. Table 4.1 summarizes the results.

Table 4.1: Normalized mean wind velocity magnitude within the circular region of interest for different layouts and radii.

Layout / Radius (m)	5	10	15	20
Reference	1.30	1.29	1.27	1.26
Layout 1	1.18	1.17	1.15	1.14
Layout 2	1.23	1.21	1.19	1.17
Layout 3	1.32	1.31	1.29	1.27
Layout 4	0.65	0.64	0.63	0.62

According to the results, for the wind direction of 147°, the mean wind velocity within the circular region is different across the layouts, with Layout 4 showing the lowest values, followed by Layouts 1 and 2 and the reference layout and Layout 3 having the highest.

The blockage profiles that correspond to this wind direction are shown in Figure 4.11

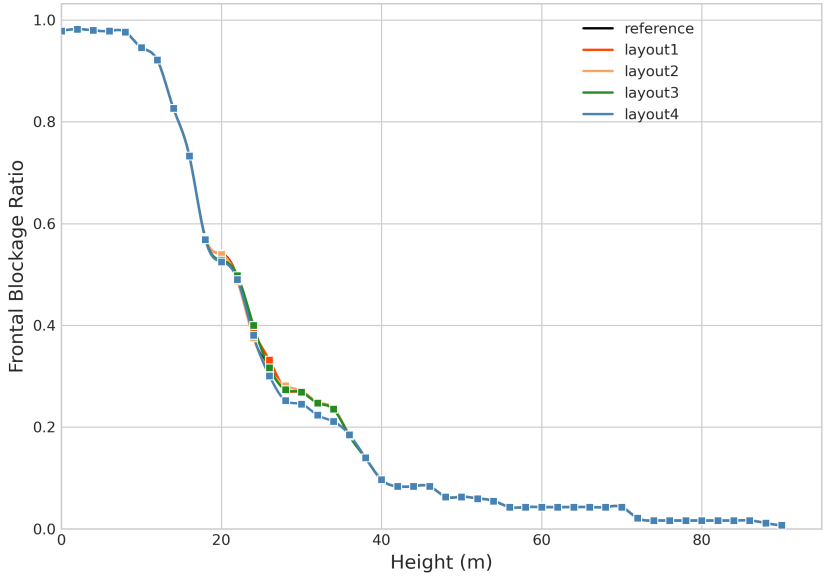

(a) Frontal blockage ratio as a function of height for a wind direction of $147°$.

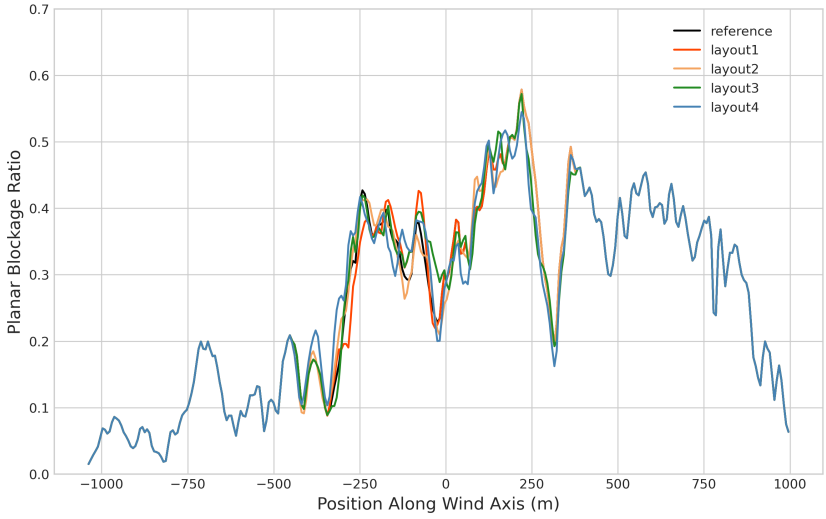

(b) Planar blockage ratio as a function of position for a wind direction of $147°$.

Figure 4.11: Blockage ratio profiles for the reference layout and modified layouts for a wind direction of $147°$.

Although all layouts show a similar trend in the frontal blockage ratios profiles, differences can be spotted by focusing on specific heights, especially in 25-35 meters range. For this reason, a representative frontal blockage metric was computed by averaging the frontal blockage ratio over the height range 25-35 m.

The planar blockage ratio profiles show a clearer distinction between the layouts. Focusing on a location at $L = 50$ m upstream of the ROI entry location, the mean planar blockage ratio was calculated for a cross-wind section of $w = 250$ m. For each layout, the resulting relationships between U_{ROI} and the blockage ratios are shown in Figures 4.12 and 4.13 for different ROI radii R.

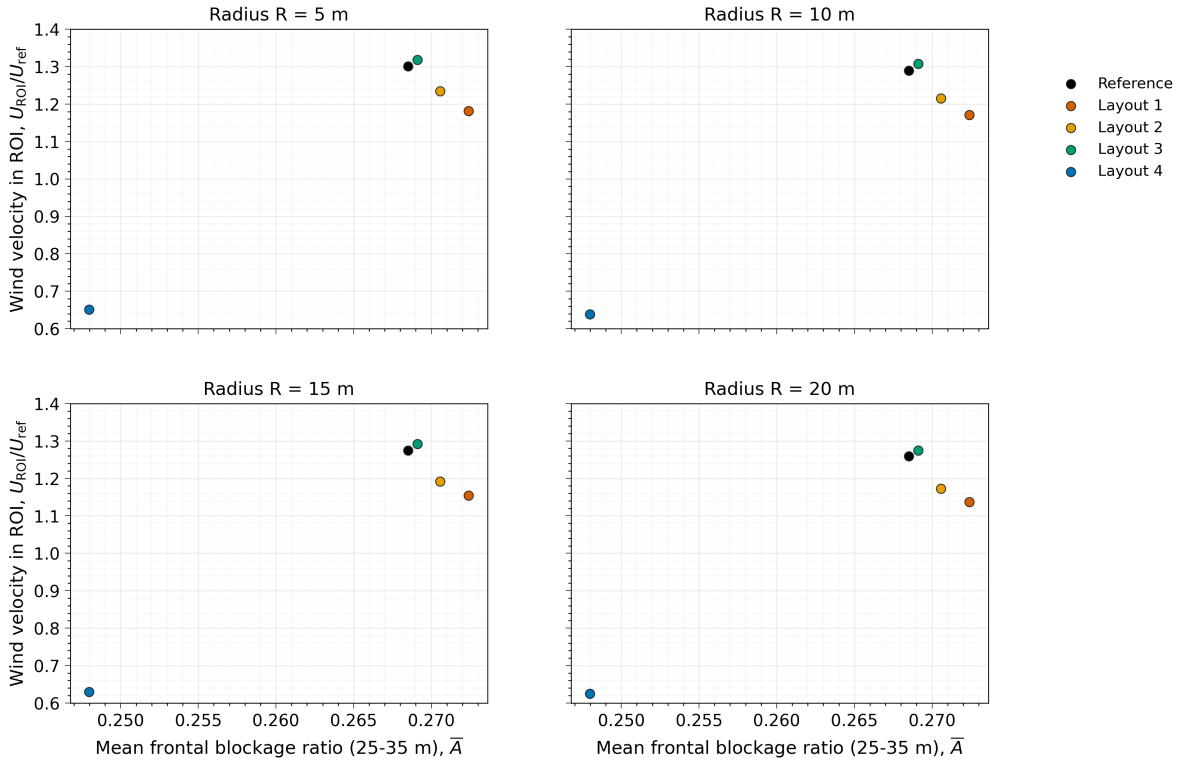

Figure 4.12: Mean wind velocity in the ROI, U_{ROI} vs the mean frontal blockage ratio (averaged over the selected height range), shown for different ROI radii R.

The frontal blockage plots (Figure 4.12) show a distinct pattern across all ROI radii. Reference, Layout 1, Layout 2 and Layout 3 are concentrated in a narrow range of frontal blockage values, forming a cluster. Within this, the points suggest an inverse relationship, where higher frontal blockage corresponds to lower normalized mean wind velocity. In contrast, Layout 4 is clearly separated from the other layouts, corresponding to the lowest frontal blockage ratio with the lowest velocity. Because of this separation, Layout 4 has a strong influence on the apparent overall trend when all five layouts are considered together. Therefore, the trend observed when all five layouts are included should not be interpreted as a general behavior across all layouts. Instead, it indicates that Layout 4 is affected by an additional mechanism that is not fully captured by the frontal blockage ratio alone. A possible explanation for this offset is the relative position of the ROI with respect to the surrounding buildings in Layout 4.

To quantify the relationships observed in Figure 4.12, the Pearson correlation coefficient (r) and the coefficient of determination (R^2) of a linear fit were calculated for each ROI radius. Since Layout 4 is separated from the other layouts and might strongly influence the overall trend, the statistics were evaluated both for the full dataset and for when excluding Layout 4.

The corresponding results are presented in Table 4.2.

Table 4.2: Linear-fit statistics for the relationship between ROI wind velocity and frontal blockage ratio at different ROI radii.

Dataset	Radius R (m)	Pearson coefficient r	Coefficient of determination R^2
All layouts	5	0.94	0.88
	10	0.94	0.88
	15	0.94	0.88
	20	0.94	0.87
Excluding Layout 4	5	-0.96	0.93
	10	-0.96	0.91
	15	-0.95	0.90
	20	-0.95	0.90

Results show that Layout strongly affects the relationship between mean velocities and frontal blockage, since including all layouts leads to a positive relationship, whereas excluding Layout 4 shows a strong negative relationship. From a physical perspective, the negative relationship observed for the clustered layouts is consistent with the expected sheltering effect, where increased blockage reduces the wind speed (Mittal et al., 2018; Stathopoulos & Wu, 1995). Layout 4 deviates from the other layouts because the ROI is located in the wake region of the relocated ME building, which provides additional sheltering and reduces the wind velocity inside the ROI, as shown in Appendix section A.6.

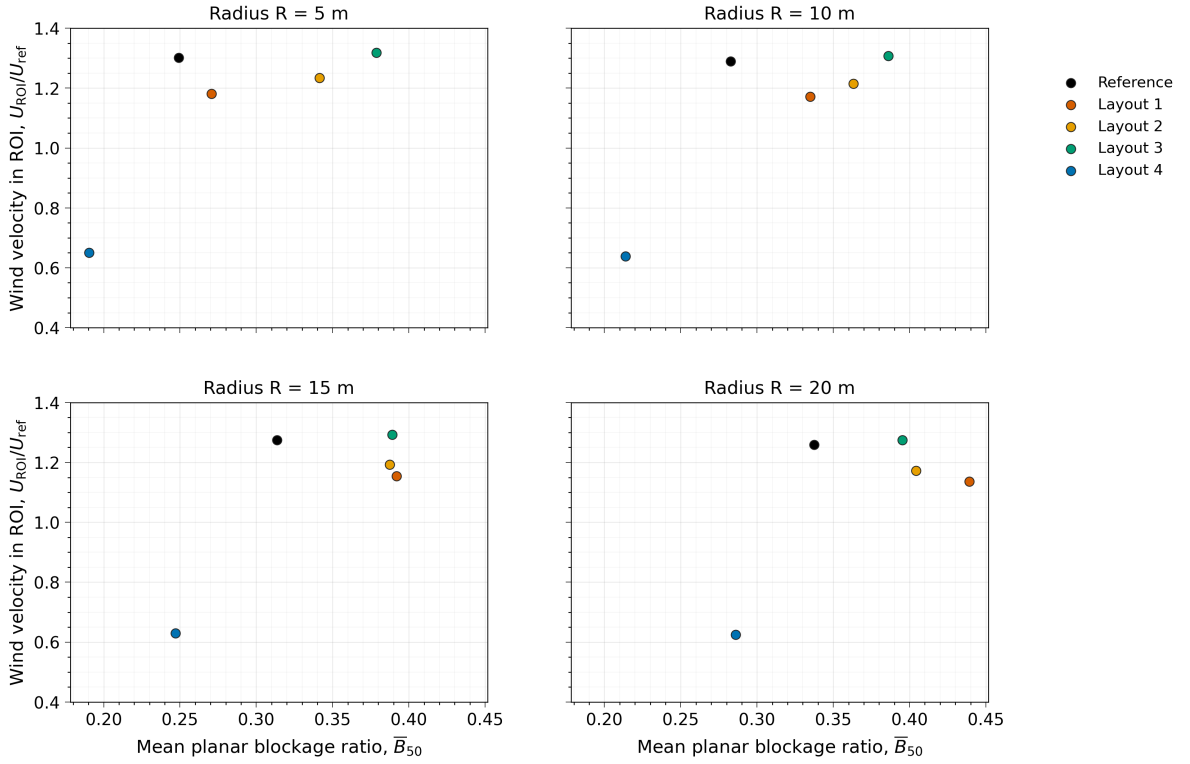

Figure 4.13: Mean wind velocity in the ROI, U_{ROI} vs the mean planar blockage ratio over a section $L = 50$ m upstream for different radii R.

The planar blockage plots (Figure 4.13) show a more scattered pattern of points. Reference, Layout 1, Layout 2 and Layout 3 are again grouped together. For smaller radii, the points suggest a weak positive relation while for larger radii the distribution becomes more spread. Similar to frontal blockage plots, Layout 4 has a much lower planar blockage ratio value.

As for the frontal blockage, the Pearson correlation coefficient (r) and the coefficient of determination

(R^2) were computed for each radius, as presented in Table 4.3.

Table 4.3: Linear-fit statistics for the relationship between ROI wind velocity and planar blockage ratio at different ROI radii.

Dataset	**Radius R (m)**	**Pearson coefficient r**	**Coefficient of determination R^2**
All layouts	5	0.75	0.56
	10	0.81	0.66
	15	0.79	0.62
	20	0.68	0.46
Excluding Layout 4	5	0.33	0.11
	10	0.00	0.00
	15	-0.48	0.23
	20	-0.76	0.58

When all layouts are included, the Pearson correlation coefficient indicates a moderate positive linear association between the planar blockage ratio and $U_{\mathrm{ROI}}/U_{\mathrm{ref}}$ and the corresponding coefficients of determination show that the linear fit explains a moderate part of the observed variation in the ROI wind velocity for all radii. Excluding Layout 4 shows a weaker blockage-velocity relation, which strongly depends on the radius, ranging from very weak positive to negative values. The linear fit is not consistent, indicating that planar blockage alone is insufficient to explain the variations in the wind.

For both blockage ratios, it should be noted that the number of data points is small. As a result, the correlation is sensitive to individual cases and can not fully describe the observed trends.

The analysis presented in this section focuses on the selected wind direction of 147°, which was identified as the most relevant case for the region of interest. For the remaining wind directions, the corresponding frontal and planar blockage-ratio plots for all layouts are included in Appendix A.8.

5

Conclusions and Recommendations

This thesis investigated how changes in the spatial arrangement of buildings influence pedestrian-level wind flow patterns. To address this problem, the TU Delft campus was used as a case study and a set of hypothetical modified layouts was constructed by relocating groups of buildings. For each layout, steady-state RANS simulations were performed to assess the resulting changes in pedestrian-level wind flow and discomfort patterns. The final conclusions are structured around the main research question and the corresponding sub-questions, followed by recommendations for future research.

5.1. Conclusions

The central research question addressed in this thesis was: *How do changes in the spatial arrangement of buildings influence pedestrian-level wind flow patterns on the TU Delft campus?* To address this question, a set of sub-questions was formulated. Below, each of these questions is answered, based on the findings of the study.

How does the existing campus geometry affect the wind flow at the pedestrian level?

In the TU Delft campus the pedestrian-level wind flow is affected by the arrangement and the height of the buildings. Due to the orientation of the campus, the approaching flow is guided differently depending on wind direction. For wind directions that are more aligned with the axis of the main corridor (e.g., the selected critical case of $147°$), the flow is channelled through the open central space, leading to locally increased pedestrian-level wind speeds. In contrast, lower wind speeds are generally observed in sheltered spaces between the buildings and in leeward regions behind them. Building height is a crucial factor in determining pedestrian-level wind conditions, as for most of the simulated wind directions, elevated wind speeds and turbulence levels are observed around EEMCS and SW2, which are the tallest structures in the study area. These flow characteristics are evident in the spatial distribution of wind discomfort risk. The highest wind discomfort probabilities at pedestrian height is concentrated around the EEMCS and SW2 buildings, where higher discomfort probabilities are related to elevated wind speed and TKE levels. A lower-intensity discomfort region is also observed in the main open space of the campus between EEMCS and CEG.

How do modifications in building arrangement influence the wind flow patterns and which areas of the campus experience the most significant changes?

The results show that building rearrangement modifies pedestrian-level wind flow mainly through local changes in wind speed and turbulence, primarily driven by the relocation of the tallest buildings. Modifications that involve the rearrangement of tall buildings, such as EEMCS and SW2 lead to changes in the pedestrian wind flow as they redistribute downwash-driven acceleration and high-turbulence zones around them. These changes are not always limited to the immediate surroundings of the relocated

buildings, but can also extend into the main central open corridor of the campus. In cases where building relocation creates narrower passages, higher pedestrian-level wind speeds are observed, as the flow is channelled through these openings. The low-speed regions are redistributed between the reference and modified layouts, in places where relocated buildings create less exposed areas to the wind flow. A similar redistribution is found for turbulence. However, the changes in TKE are more localized and tend to move with the new positions of the tall buildings. Across the modified layouts, the largest differences in velocity magnitude relative to the reference case occur mainly in the central campus, near the modified building locations. In general, higher wind speeds are observed near relocated EEMCS tower and SW2 building, while in certain layouts, more sheltered areas show reduced pedestrian-level wind speeds. Overall, Layout 4 shows the most spatially extensive changes relative to the reference configuration, which is consistent with the fact that it includes the largest number of building rearrangements.

What are the implications of the observed wind flow patterns for pedestrian wind comfort in each layout?

The observed flow patterns are directly reflected in the pedestrian wind comfort results. Areas with higher discomfort risk align with regions of increased TKE, mainly following the relocation of EEMCS and SW2. The spatial distribution of these regions varies between layouts. In general, the discomfort zones tend to extend over a larger area when the tall buildings are placed in more exposed locations, relative to the inflow directions. The highest risk for pedestrian wind discomfort is mainly observed around the building edges and it is also present in the main open area of the campus, with lower intensity. In the case of the EEMCS tower, the results suggest that a relocation closer to other buildings can limit the spatial extent of the discomfort zone, by providing more shielding. Comparing the modified layouts overall, the results indicate that the building rearrangements mainly redistribute pedestrian wind discomfort zones across the campus, with conditions improving in some areas and worsening in others. Focusing on the main central part of the campus, which is an intensively used pedestrian area, Layout 3 shows the clearest improvement in pedestrian wind comfort conditions.

How does the building blockage contribute to the observed changes in local pedestrian-level wind flow?

The wind direction that produces the highest wind speeds in the main open space of the campus is 147°. For this direction, the analysis shows that mean wind velocity in the region of interest is influenced by the upstream geometric blockage, however the consistency of this relationship depends on the blockage metric used. The frontal blockage ratio shows a clear inverse trend for the reference layout and Layouts 1, 2 and 3, with increased blockage associated with lower wind velocity. Layout 4 deviates from this trend, suggesting that additional local geometric factors also affect the local wind flow. In particular, the region of interest is located much closer to the nearby building and in a more sheltered location created by the surrounding buildings, leading to lower velocities. In contrast, the planar blockage ratio shows a weaker relationship with the wind velocity, with a more scattered behavior across ROI radii. This suggests that an averaged planar blockage ratio alone is insufficient to capture the local wind response in the ROI.

In summary, although the modified layouts considered in this thesis are hypothetical, the results can provide insight into the underlying mechanisms through which changes in the built environment can affect pedestrian-level wind flow. The results highlight that building arrangement is a key factor in determining the pedestrian wind discomfort, affecting both the intensity and the spatial extent of discomfort zones. Therefore, integrating appropriate design decisions in the planning of the urban environment is essential for providing comfortable and safe outdoor spaces.

5.2. Recommendations

This study has several limitations that affect the interpretation of the results indicate directions for future work.

Regarding the inflow conditions, the selection of wind directions was based on data from the Delfshaven weather station, which was chosen because it provides a long data record and is relatively close to Delft. However, the measurements at this station may be influenced by local topography and urban geometry and as a result they do not fully represent the wind conditions over the TU Delft campus. In addition, the use of 12 inflow directions remains an approximation of the wind conditions in the area. Future studies should therefore consider using campus-based wind measurements and assess the sensitivity of the results to the number of simulated wind directions.

The wind comfort assessment in this study was based on a combined velocity–TKE exceedance criterion with threshold parameters ($\alpha = 0.4$, $\beta = 0.08$), adopted from previous work (Patil & García-Sánchez, 2025). While this provides a consistent framework across the different layouts, the selected values are not part of a standardized wind comfort criterion. Therefore, different parameter choices can change the resulting discomfort probabilities. In addition, since discomfort is defined through the joint exceedance of both thresholds, the criterion does not automatically capture all situations in which only one of the two quantities reaches elevated levels. For this reason, the criterion should be interpreted as a comparative indicator and be evaluated carefully, through comparison with observations.

The modified layouts in this thesis were generated by moving groups of buildings, while all the other geometric surfaces, including vegetation and water remained in their original positions. This was appropriate for isolating the effect of building arrangement, however it can introduce inconsistencies between the relocated buildings and the underlying surface types. For example, a relocated building might be placed partially over areas that were previously water or vegetation. Since these surface types are assigned different roughness properties that affect the wind velocity, this mismatch may influence the pedestrian-level results around the building. As a result, adjusting these surfaces together with the buildings relocation could lead to a more realistic scenarios.

For the blockage-ratio analysis, an important limiting factor is the small number of data points, since the correlations were based on only five mean velocities. As a result, the observed relationships are sensitive to individual cases. In addition, the planar blockage analysis was evaluated for a selected upstream section of $50\ \mathrm{m}$. Future work could test different upstream distances and include additional velocity samples. The analysis can also be extended to other wind directions in order to assess the generality of the blockage ratio–velocity relationships.

Another important note is that each modified layout includes multiple geometric changes simultaneously. Moving buildings changes not only their position, but also their orientation to the inflow, their exposure and their interaction with surrounding buildings. The resulting flow field is therefore a combined response, which makes it difficult to isolate the effect of individual geometric factors. Future work could address this by applying smaller and more targeted modifications in selected locations that experience unfavorable pedestrian wind comfort in order to assess the sensitivity of local wind conditions more systematically.

Finally, selected cases could be further examined using alternative modelling approaches (e.g., unsteady RANS or LES) to better capture unsteady flow effects. While the present work evaluates time-averaged wind speed and turbulence quantities using steady RANS, these approaches can provide time-resolved information on velocity fluctuations. These simulations would therefore enable assessment of wind-speed variability, especially in regions with strong turbulence and location where flow separation occurs. Although substantial changes in the mean-flow patterns are not necessarily expected, the additional information on fluctuations could improve the identification of areas with a high risk of wind discomfort.

References

Adamek, K., Vasan, N., Elshaer, A., English, E., & Bitsuamlak, G. (2017). Pedestrian level wind assessment through city development: A study of the financial district in toronto. *Sustainable Cities and Society*, *35*, 178–190. https://doi.org/https://doi.org/10.1016/j.scs.2017.06.004

ASHRAE. (2005). Airflow around buildings [Often listed as Chapter 16 in the 2005 SI edition]. In *Ashrae handbook—fundamentals*. American Society of Heating, Refrigerating; Air-Conditioning Engineers. Retrieved February 8, 2026, from https://oss.jishulink.com/caenet/forums/upload/2013/12/10/388/147581638606778.pdf

Baş, H., Andrianne, T., & Reiter, S. (2024). City configurations to optimise pedestrian level ventilation and wind comfort. *Sustainable Cities and Society*, *114*, 105745. https://doi.org/https://doi.org/10.1016/j.scs.2024.105745

Biljecki, F., Ledoux, H., & Stoter, J. (2016). An improved lod specification for 3d building models. *Computers, Environment and Urban Systems*, *59*, 25–37. https://doi.org/https://doi.org/10.1016/j.compenvurbsys.2016.04.005

Blocken, B., Janssen, W., & van Hooff, T. (2012). Cfd simulation for pedestrian wind comfort and wind safety in urban areas: General decision framework and case study for the eindhoven university campus. *Environmental Modelling & Software*, *30*, 15–34. https://doi.org/https://doi.org/10.1016/j.envsoft.2011.11.009

Blocken, B., Stathopoulos, T., & van Beeck, J. (2016). Pedestrian-level wind conditions around buildings: Review of wind-tunnel and cfd techniques and their accuracy for wind comfort assessment. *Building and Environment*, *100*, 50–81. https://doi.org/https://doi.org/10.1016/j.buildenv.2016.02.004

Blocken, B. (2015). Computational fluid dynamics for urban physics: Importance, scales, possibilities, limitations and ten tips and tricks towards accurate and reliable simulations [Fifty Year Anniversary for Building and Environment]. *Building and Environment*, *91*, 219–245. https://doi.org/https://doi.org/10.1016/j.buildenv.2015.02.015

Britter, R., & Hanna, S. (2003). Flow and dispersion in urban areas. *ARFM*, *35*, 469–496. https://doi.org/10.1146/annurev.fluid.35.101101.161147

Chen, L., Hang, J., Sandberg, M., Claesson, L., Di Sabatino, S., & Wigo, H. (2017). The impacts of building height variations and building packing densities on flow adjustment and city breathability in idealized urban models. *Building and Environment*, *118*, 344–361. https://doi.org/10.1016/j.buildenv.2017.03.042

Chen, X., Hu, H., Xu, Z., Wu, Z., Ma, R., & Wang, X. (2025). Wind comfort criteria and numbers of wind directions: The dual impact mechanism on pedestrian wind comfort evaluation in qingdao, china. *Building and Environment*, *280*, 113103. https://doi.org/https://doi.org/10.1016/j.buildenv.2025.113103

City of London Corporation. (2019, August). *Wind microclimate guidelines* [Technical guidance for wind microclimate studies accompanying planning applications (August 2019)]. Retrieved February 12, 2026, from https://www.cityoflondon.gov.uk/assets/Services-Environment/wind-microclimate-guidelines.pdf

Delft High Performance Computing Centre. (2024). DelftBlue Supercomputer (Phase 2).

Franke, J. (2006). Recommendations of the COST action C14 on the use of CFD in predicting pedestrian wind environment. *Proceedings of the Fourth International Symposium on Computational Wind Engineering (CWE2006)*, 529–532.

Franke, J., Hellsten, A., Schlünzen, H., & Carissimo, B. (2007). *Best practice guideline for the cfd simulation of flows in the urban environment* (COST European Cooperation in Science and Technology). COST Action 732. https://hal.science/hal-04181390

García-Sánchez, C., Vitalis, S., Paden, I., & Stoter, J. (2021). The impact of level of detail in 3d city models for cfd-based wind flow simulations. *The International Archives of the Photogrammetry,*

Remote Sensing and Spatial Information Sciences, *XLVI-4/W4-2021*, 67–72. https://doi.org/10.5194/isprs-archives-XLVI-4-W4-2021-67-2021

Hågbo, T.-O., Giljarhus, K. E. T., & Hjertager, B. H. (2021). Influence of geometry acquisition method on pedestrian wind simulations. *Journal of Wind Engineering and Industrial Aerodynamics*, *215*, 104665. https://doi.org/https://doi.org/10.1016/j.jweia.2021.104665

Intergovernmental Panel on Climate Change (IPCC). (2021, August). *Climate change widespread, rapid, and intensifying – ipcc* [IPCC Working Group I press release (AR6, The Physical Science Basis)]. Retrieved February 18, 2026, from https://www.ipcc.ch/2021/08/09/ar6-wg1-20210809-pr/

Keskinen, J.-P., & Hellsten, A. (2025). Ensembles in urban large eddy simulations with changing wind direction [Article number 26; published online 3 July 2025]. *Boundary-Layer Meteorology*, *191*, 26. https://doi.org/https://doi.org/10.1007/s10546-025-00916-x

Kubota, T., Miura, M., Tominaga, Y., & Mochida, A. (2008). Wind tunnel tests on the relationship between building density and pedestrian-level wind velocity: Development of guidelines for realizing acceptable wind environment in residential neighborhoods. *Building and Environment*, *43*(10), 1699–1708. https://doi.org/10.1016/j.buildenv.2007.10.015

Kundu, P. K., Cohen, I. M., & Dowling, D. R. (2012). *Fluid mechanics* (5th ed.). Academic Press.

Launder, B., & Spalding, D. (1974). The numerical computation of turbulent flows. *Computer Methods in Applied Mechanics and Engineering*, *3*(2), 269–289. https://doi.org/https://doi.org/10.1016/0045-7825(74)90029-2

Lawson, T. V. (1978). The wind content of the built environment. *Journal of Wind Engineering and Industrial Aerodynamics*, *3*(2-3), 93–105. https://doi.org/10.1016/0167-6105(78)90002-8

Mckay, M., Beckman, R., & Conover, W. (1979). A comparison of three methods for selecting vales of input variables in the analysis of output from a computer code. *Technometrics*, *21*, 239–245. https://doi.org/10.1080/00401706.1979.10489755

Melbourne, W. H. (1978). Criteria for environmental wind conditions. *Journal of Wind Engineering and Industrial Aerodynamics*, *3*(2-3), 241–249. https://doi.org/10.1016/0167-6105(78)90013-2

Mittal, H., Sharma, A., & Gairola, A. (2018). A review on the study of urban wind at the pedestrian level around buildings. *Journal of Building Engineering*, *18*, 154–163. https://doi.org/https://doi.org/10.1016/j.jobe.2018.03.006

NEN. (2006). Nen 8100:2006 nl — windhinder en windgevaar in de gebouwde omgeving [Dutch standard; Royal Netherlands Standardization Institute (NEN)].

Oke, T. R., Mills, G., Christen, A., & Voogt, J. A. (2017). *Urban climates*. Cambridge University Press.

Open Geospatial Consortium. (2012). City geography markup language (citygml) encoding standard, version 2.0.0. https://www.ogc.org/standards/citygml/

OpenFOAM Foundation. (2021). *Openfoam user guide, version 7* [Accessed: 2025-01-10]. OpenFOAM Foundation. https://openfoam.org

OpenStreetMap contributors. (2026). *Openstreetmap* [Accessed via OpenStreetMap]. Retrieved February 17, 2026, from https://www.openstreetmap.org/

Park, S.-J., Kim, J.-J., Choi, W., Kim, E.-R., Song, C.-K., & Pardyjak, E. (2020). Flow characteristics around step-up street canyons with various building aspect ratios. *Boundary-Layer Meteorology*, *174*. https://doi.org/10.1007/s10546-019-00494-9

Patil, A., & García-Sánchez, C. (2025). Quantifying the impact of urban geometric detail for urban air mobility risk forecasting. *Sustainable Cities and Society*, *132*, 106750. https://doi.org/https://doi.org/10.1016/j.scs.2025.106750

Peters, R., Dukai, B., Vitalis, S., van Liempt, J., & Stoter, J. (2022). Automated 3D reconstruction of LoD2 and LoD1 models for all 10 million buildings of the Netherlands. *Photogrammetric Engineering and Remote Sensing*, *88*(3), 165–170. https://doi.org/10.14358/PERS.21-00032R2

Reiter, S. (2010). Assessing wind comfort in urban planning. *Environment and Planning B: Planning and Design*, *37*, 857–873. https://doi.org/10.1068/b35154

Richards, P., & Hoxey, R. (1993). Appropriate boundary conditions for computational wind engineering models using the k-□ turbulence model [Proceedings of the 1st International on Computational Wind Engineering]. *Journal of Wind Engineering and Industrial Aerodynamics*, *46-47*, 145–153. https://doi.org/https://doi.org/10.1016/0167-6105(93)90124-7

Soulhac, L., Garbero, V., Salizzoni, P., Mejean, P., & Perkins, R. (2009). Flow and dispersion in street intersections. *Atmospheric Environment*, *43*(18), 2981–2996. https://doi.org/https://doi.org/10.1016/j.atmosenv.2009.02.061

Stathopoulos, T. (2006). Pedestrian level winds and outdoor human comfort [Urban Civil Engineering (UCE), Impact of wind and storms on city life and built environment.]. *Journal of Wind Engineering and Industrial Aerodynamics*, *94*(11), 769–780. https://doi.org/https://doi.org/10.1016/j.jweia.2006.06.011

Stathopoulos, T., & Wu, H. (1995). Generic models for pedestrian-level winds in built-up regions. *Journal of Wind Engineering and Industrial Aerodynamics*, *54–55*, 515–525. https://doi.org/10.1016/0167-6105(94)00068-O

Stewart, I. D., & Oke, T. R. (2012). Local climate zones for urban temperature studies. *Bulletin of the American Meteorological Society*, *93*(12), 1879–1900. https://doi.org/10.1175/BAMS-D-11-00019.1

Stull, R. B. (1988). *An introduction to boundary layer meteorology*. Kluwer Academic Publishers.

To, A., & Lam, K. (1995). Evaluation of pedestrian-level wind environment around a row of tall buildings using a quartile-level wind speed descripter [Third Asian-Pacific Symposium on Wind Engineering]. *Journal of Wind Engineering and Industrial Aerodynamics*, *54-55*, 527–541. https://doi.org/https://doi.org/10.1016/0167-6105(94)00069-P

TU Delft. (2025, July). *Time capsule marks start of construction of physics on tu delft campus*. Retrieved February 15, 2026, from https://www.tudelft.nl/en/2025/tu-delft/time-capsule-marks-start-of-construction-of-physics-on-tu-delft-campus

TU Delft. (2026). *A sustainable and accessible campus* [Accessed for campus daily users and mobility context]. Retrieved February 15, 2026, from https://www.tudelft.nl/en/about-tu-delft/contact/our-campus/a-sustainable-accessible-campus

TU Delft Delta. (2019). *The ghastly winds around eemcs*. Retrieved February 15, 2026, from https://delta.tudelft.nl/en/article/series-ghastly-winds-around-eemcs

United Nations, Department of Economic and Social Affairs, Population Division. (2025). *World urbanization prospects 2025: Key messages*. Retrieved February 14, 2026, from https://population.un.org/wup/assets/Publications/undesa_pd_2024_key_messages_wup_2025.pdf

van Hooff, T., Blocken, B., & Tominaga, Y. (2017). On the accuracy of cfd simulations of cross-ventilation flows for a generic isolated building: Comparison of rans, les and experiments. *Building and Environment*, *114*, 148–165. https://doi.org/https://doi.org/10.1016/j.buildenv.2016.12.019

Zhang, X., Weerasuriya, A. U., Zhang, X., et al. (2020). Pedestrian wind comfort near a super-tall building with various configurations in an urban-like setting. *Building Simulation*, *13*, 1385–1408. https://doi.org/10.1007/s12273-020-0658-6

A

Supplementary material

A.1. Blender workflow for modified layout geometry

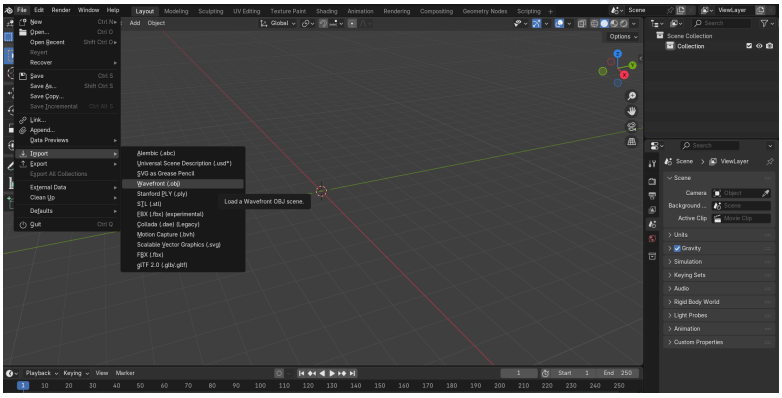

Figure A.1: (Step 1) Overview: import footprint geometry in wavefront (.obj) format.

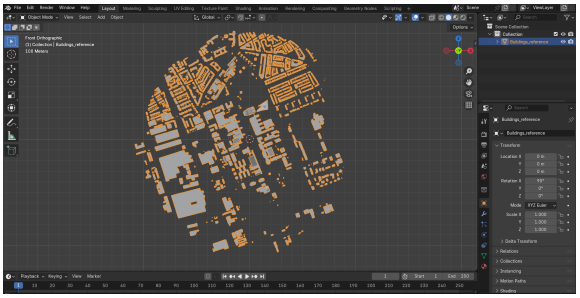

(a) Plane view of buildings in Object mode.

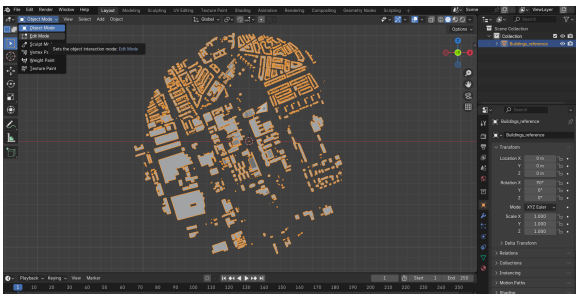

(b) (Step 2) Switch to Edit Mode.

Figure A.2: Selection setup prior to translation.

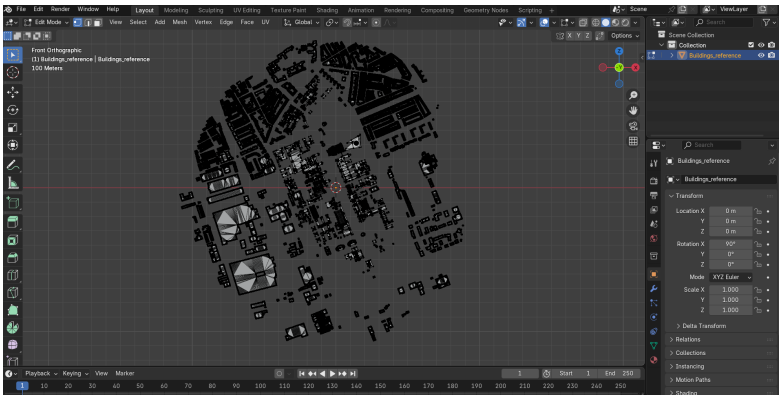

Figure A.3: (Step 3) Plane view of buildings in Edit mode.

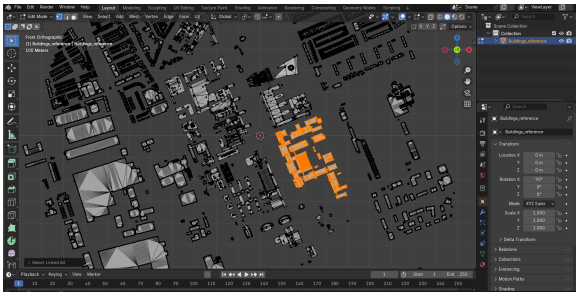

(a) (Step 4) Select edges and use `Ctrl+L` (Select Linked) to select the entire connected building mesh.

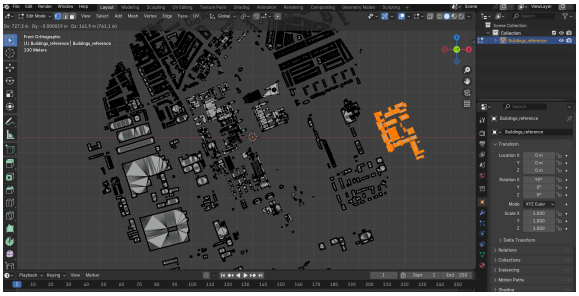

(b) (Step 4) Move and rotate the buildings using `G` (Move) and `R` (Rotate).

Figure A.4: Post-translation verification and final configuration.

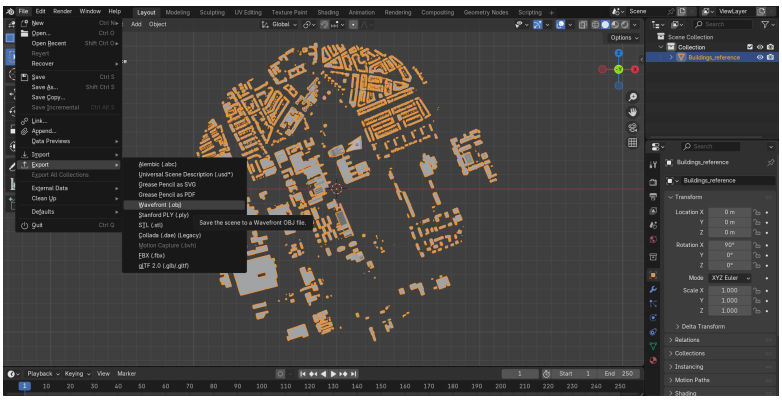

Figure A.5: (Step 5) Export geometry: select all objects (`A`) and export the modified layout as a wavefront (.obj) file.

A.2. Zoomed-in views of the central campus area

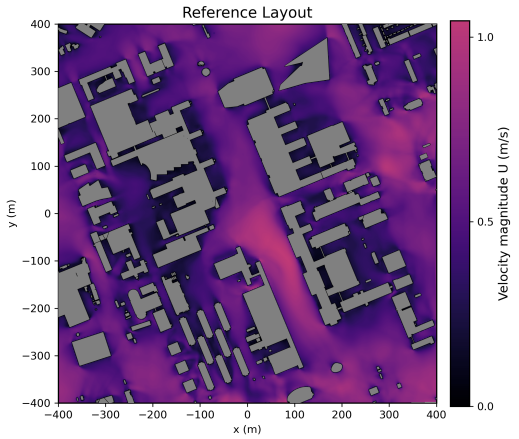

(a) Reference layout

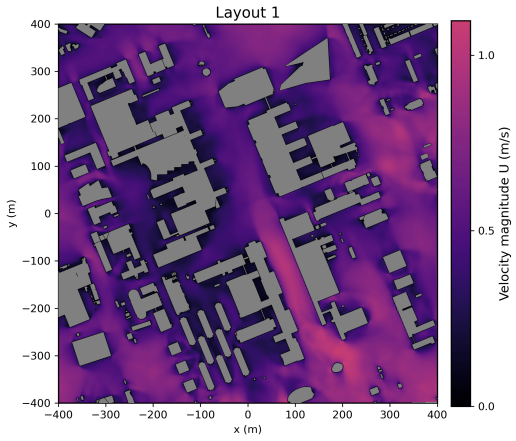

(b) Layout 1

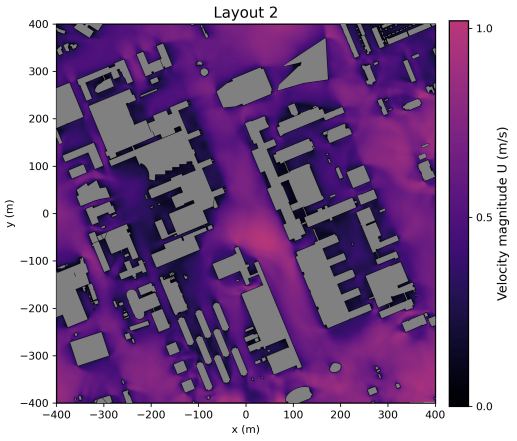

(c) Layout 2

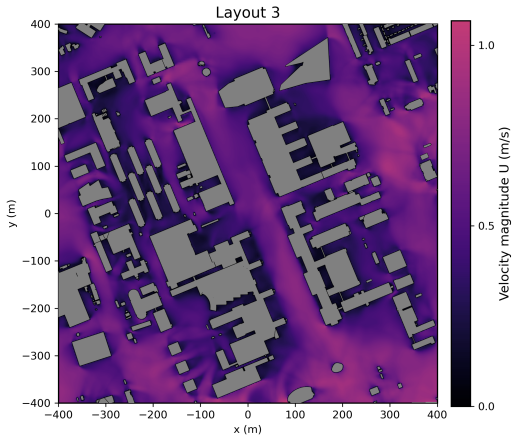

(d) Layout 3

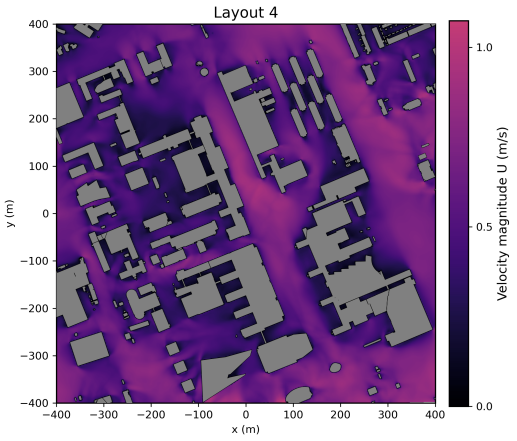

(e) Layout 4

Figure A.6: Zoomed-in views of the directionally averaged normalized wind velocity at pedestrian level in the main central area of the campus for the reference and modified layouts.

A.3. Wind field animation

To examine the directional variability of the wind flow at pedestrian level, the velocity magnitude fields were plotted for all wind directions selected in the simulation. For this an animated visualisation of the wind velocity for all wind directions. The animation can be accessed through Figure A.7.

Figure A.7: QR code linking to an animation of the pedestrian-level wind velocity fields for all simulated wind directions.

A.4. Discomfort probability maps with different α and β values

This section illustrates how the discomfort probability maps change with the choice of threshold parameters α and β used in the combined exceedance criterion:

$$U > \alpha U_{\mathrm{ref}}, \qquad k > \beta U_{\mathrm{ref}}^2.$$

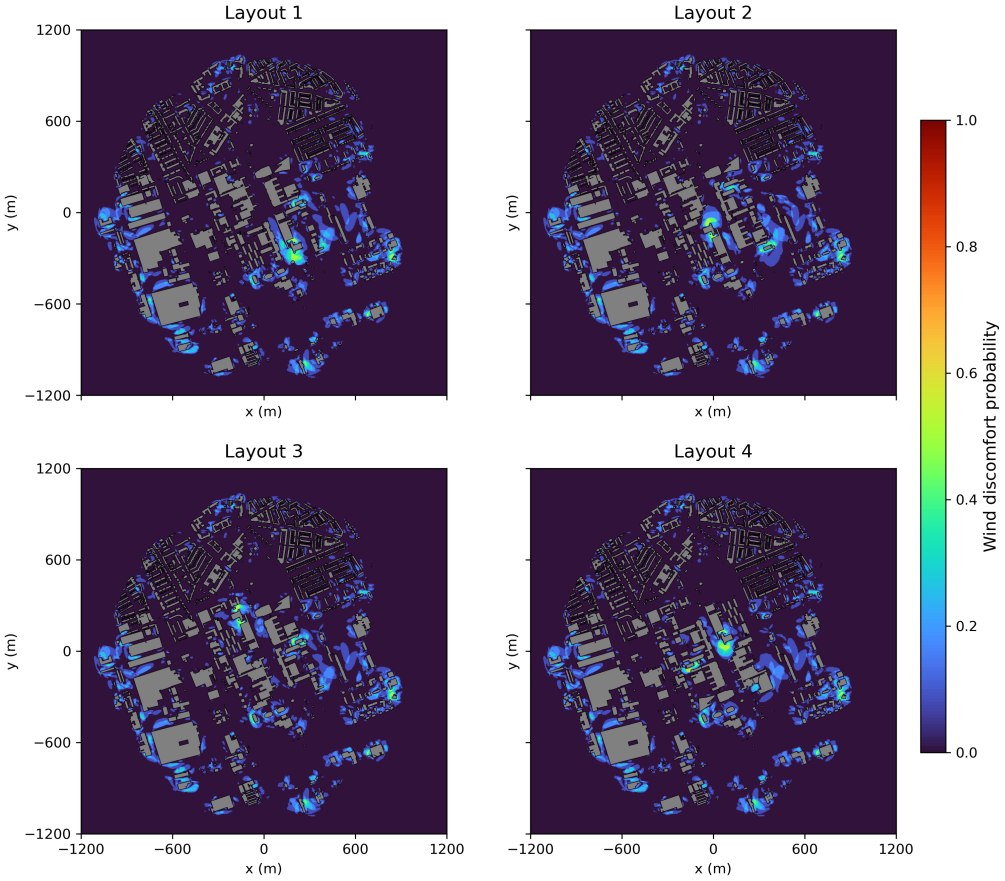

Figure A.8: Discomfort probability map computed with $\alpha = 0.1$ and $\beta = 0.08$.

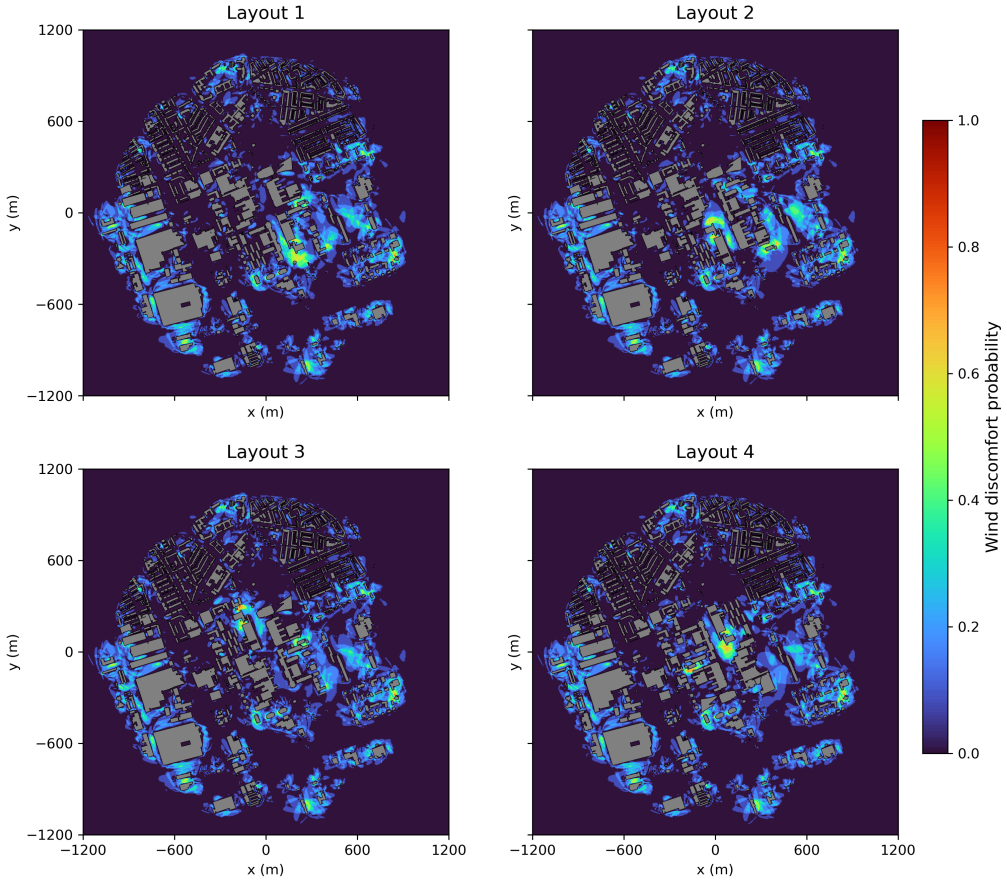

Figure A.9: Discomfort probability map computed with $\alpha = 0.4$ and $\beta = 0.06$.

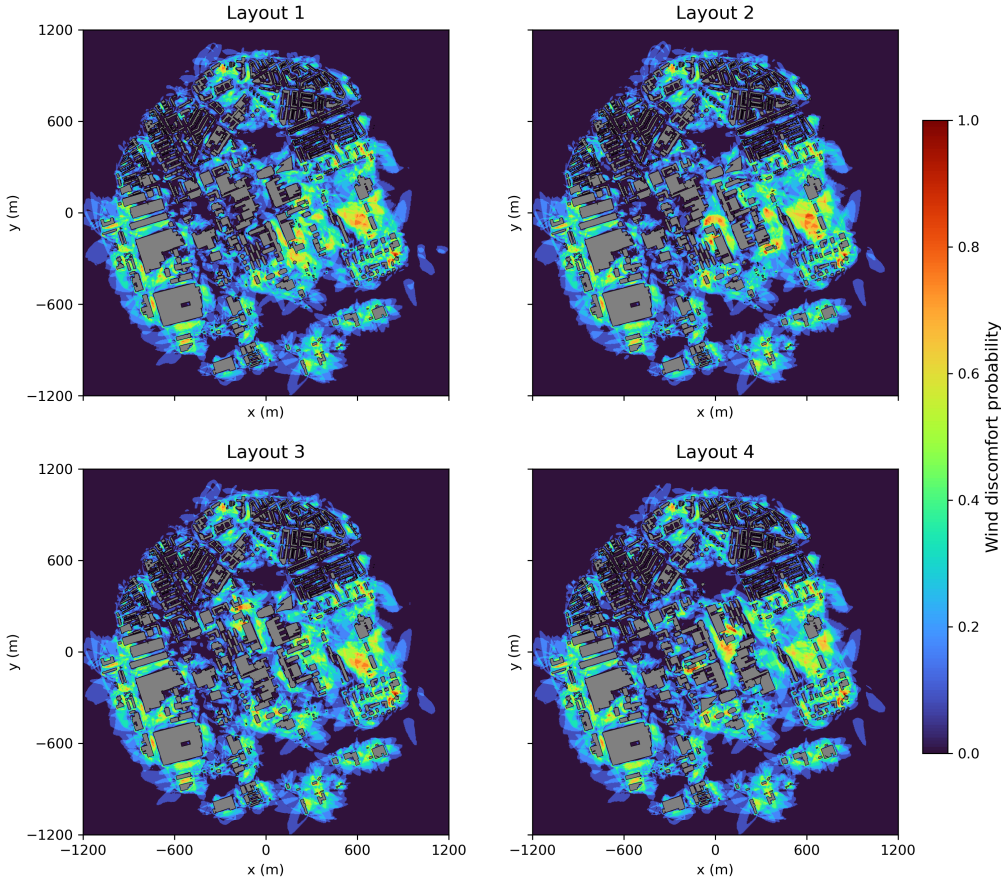

Figure A.10: Discomfort probability map computed with $\alpha = 0.4$ and $\beta = 0.04$.

A.5. Normalized wind velocities for the 147° wind direction in modified layouts

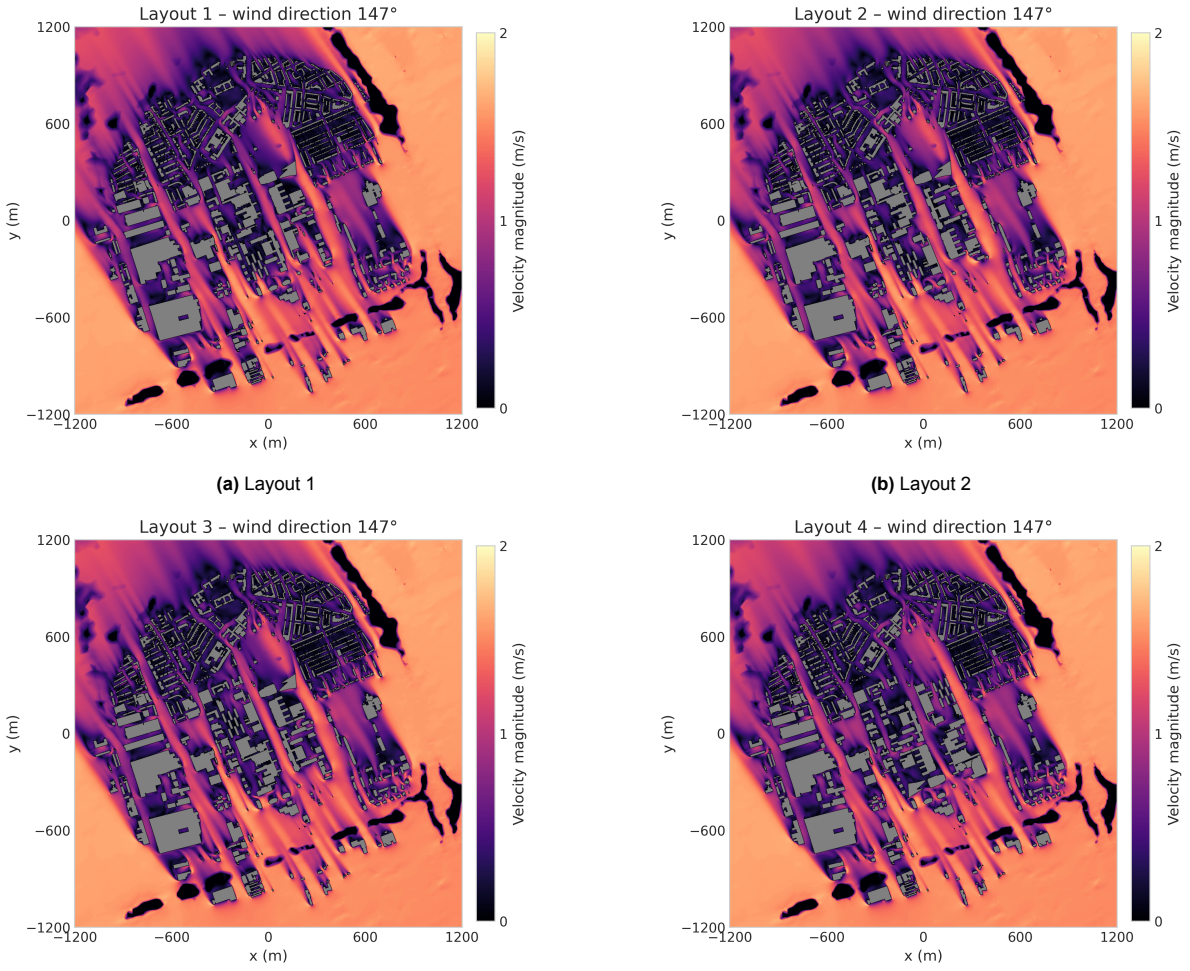

(a) Layout 1

(b) Layout 2

(c) Layout 3

(d) Layout 4

Figure A.11: Wind velocities at pedestrian height in modified layouts for 123° wind direction.

A.6. Region of Interest in Reference and modified Layouts for 147° wind direction

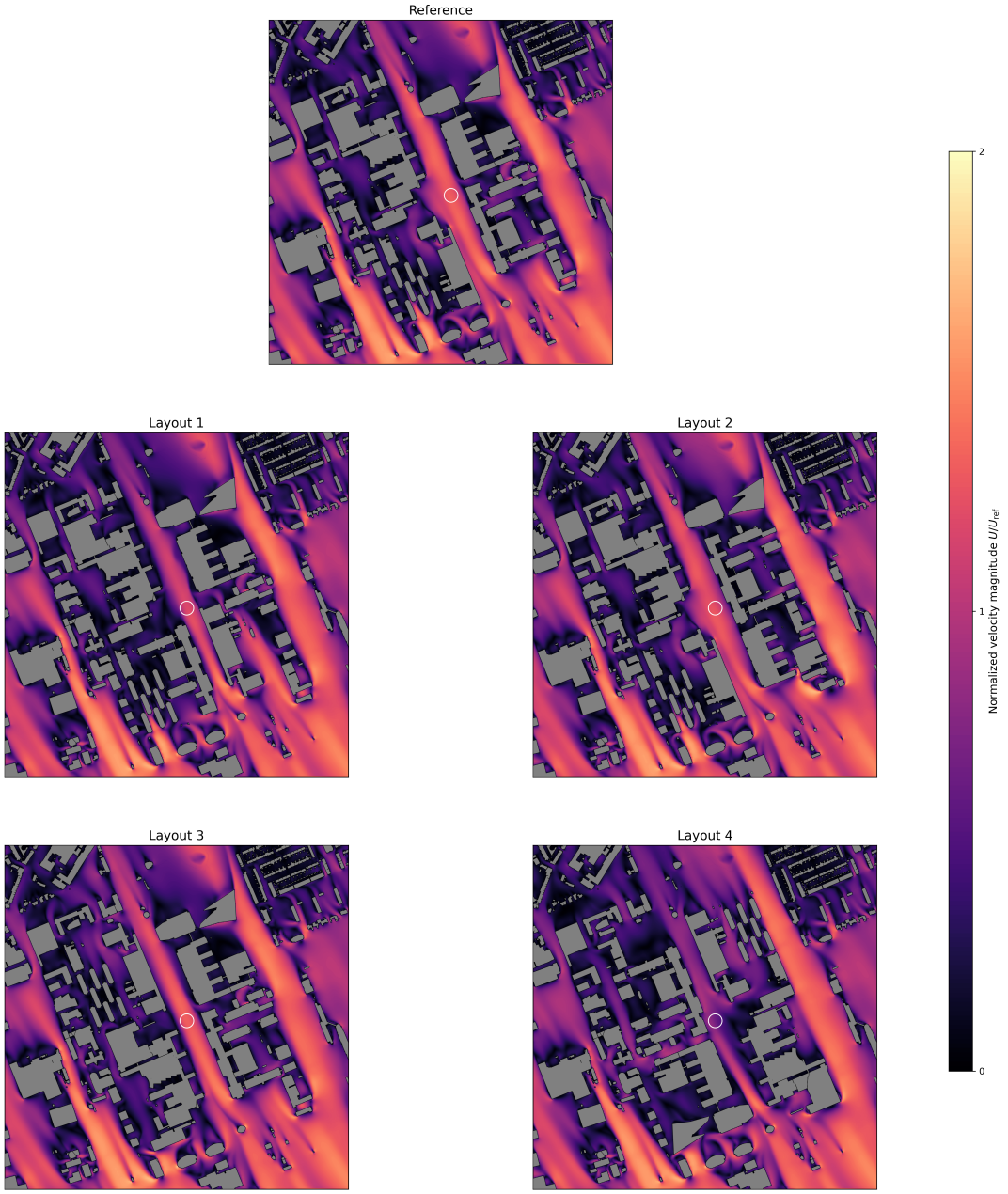

Figure A.12: Circular region of interest on the reference and modified campus layouts for 147° wind direction.

A.7. Visualization of the planar blockageratio for the modified layouts

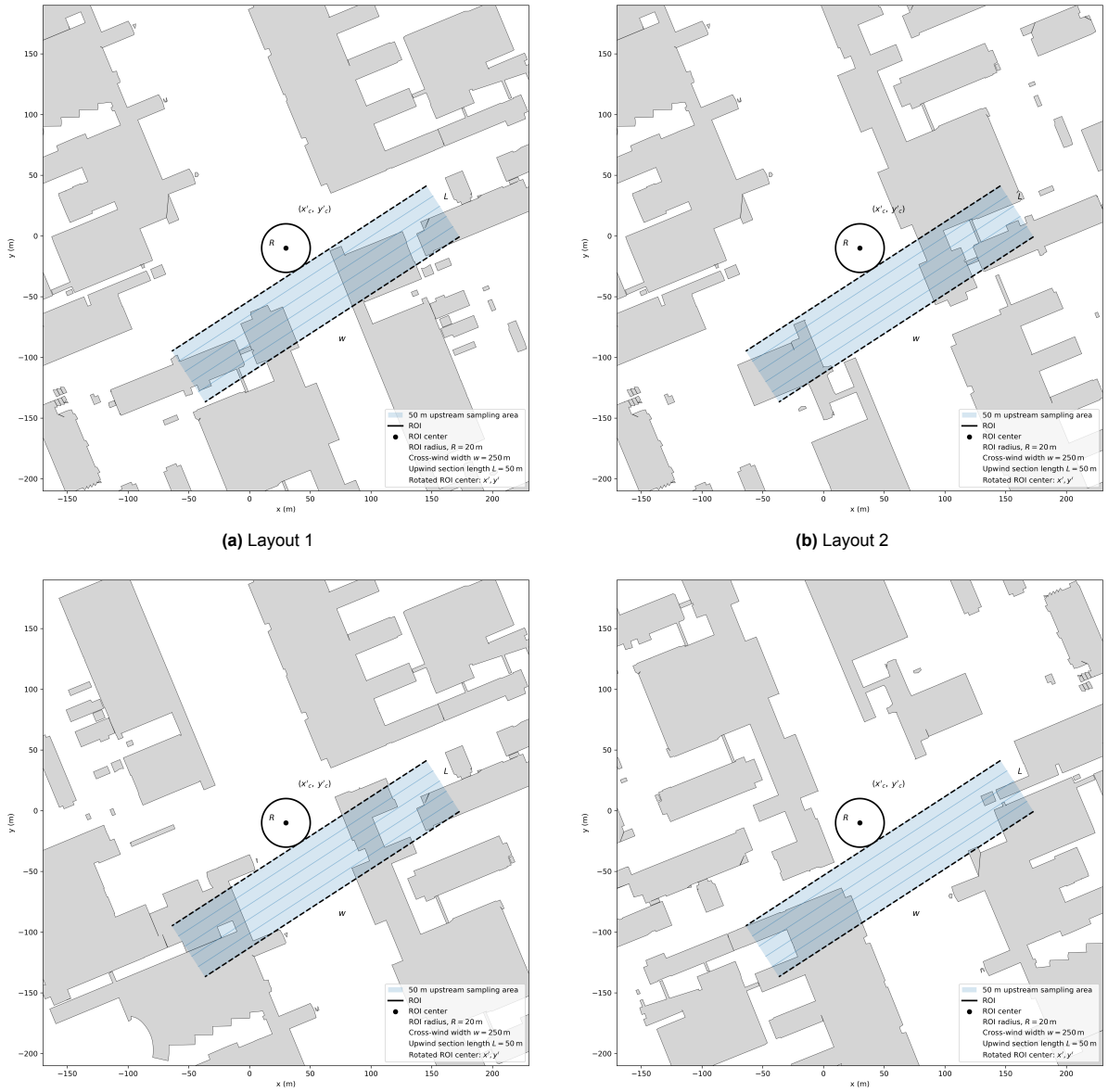

(a) Layout 1

(b) Layout 2

(c) Layout 3

(d) Layout 4

Figure A.13: Visualization of the geometric setup used in the local planar blockage-ratio analysis for the four modified layouts. Each figure shows the region of interest (ROI), the entry location x'_{entry}, the cross-wind corridor of width w, and the upstream section of length L, shown in the original campus orientation.

A.8. Blockage ratio as a function of wind direction

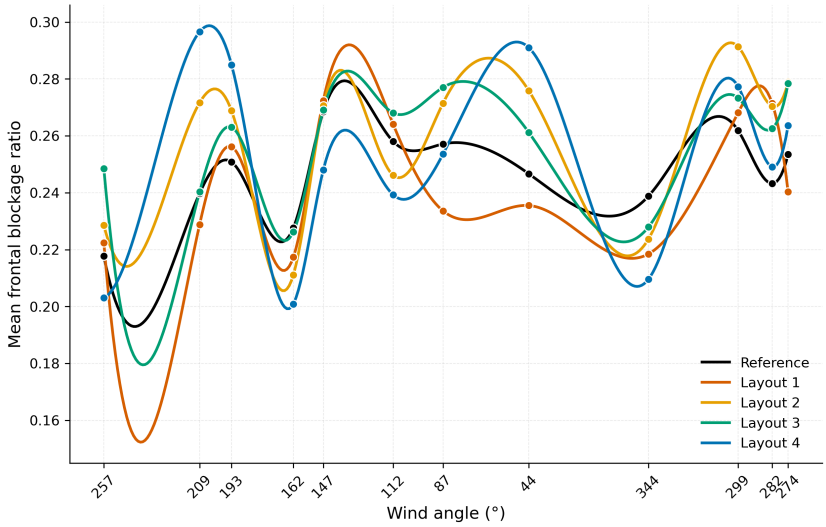

Figure A.14: Mean frontal blockage ratio as a function of meteorological wind direction for the reference and modified layouts. The frontal blockage ratio is averaged over the height range 25–35 m.

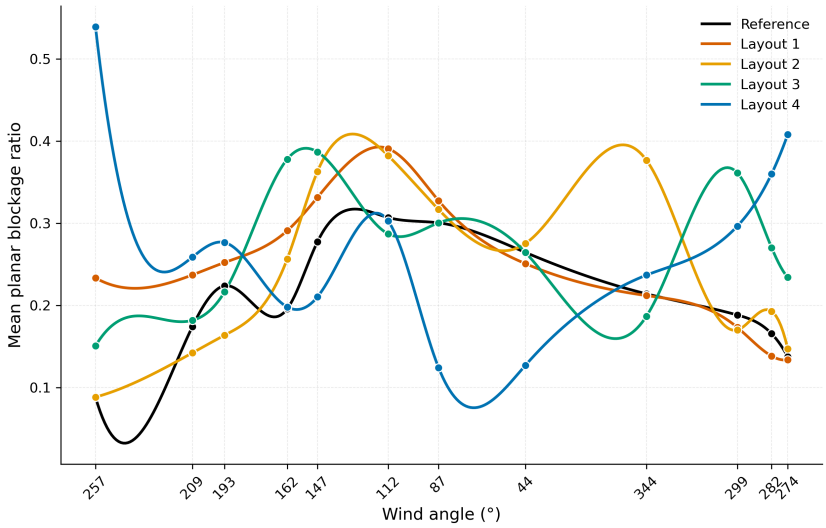

Figure A.15: Mean planar blockage ratio as a function of meteorological wind direction for the reference and modified layouts for ROI radius of 10 m.. The planar blockage ratio is computed over the 50 m upstream section of the region of interest using a corridor width of 250 m.

B

Initial approach

At the beginning of this thesis, the research was initially designed to investigate how changes in the road network influence wind flow on the TU Delft campus. The original idea was to modify the street-network geometry while keeping the other main morphological characteristics of the campus as consistent as possible, and then use the resulting layouts as input for CFD simulations.

In this initial approach, the existing road network of the TU Delft campus was first analyzed using *OSMnx*. Alternative street-network configurations were then generated using *CityStack*, with the intention of modifying the road angles while preserving the general morphological properties of the area. The next step would have been to reposition the existing buildings on the modified networks in order to create new campus layouts, which could then be used for the wind-flow simulations.

Although the first stages of this workflow were completed successfully, the resulting layouts revealed important limitations that reduced the feasibility of this approach for the purposes of the present study. In particular, the generated street-network layouts could not be controlled in a systematic way, since the tool produced a different configuration at each run even when similar settings were used. This made it difficult to isolate the effect of specific geometric changes, such as variations in street angle. In addition, the generated layouts did not preserve the overall spatial character of the TU Delft campus, which made the placement of buildings on the modified networks difficult. Finally, in many cases the generated road networks extended outside the domain, as illustrated in as illustrated in Figure B.1

(a) Modified street network 1.

(b) Modified street network 2.

Figure B.1: Alternative streetnetwork configurations of TU Delft campus generated with CityStack.

Since the layouts generated with *CityStack* could not provide input geometries in a form suitable for the present study, the methodology had to be revised. The initial idea of generating new campus configurations by modifying only the road network was therefore abandoned. Although it would in principle have been possible to alter the street angles, it was not feasible to do so while keeping the other main morphological characteristics unchanged, as originally intended. As a result, the focus of the study was shifted toward creating alternative layouts by rearranging the existing buildings within the domain.

As a first attempt to generate modified building layouts, a random rearrangement approach was tested. For this purpose, a script was developed that swapped buildings randomly between predefined grid cells. The domain was first divided into a selected number of grid cells, after which a prescribed number of random swaps was performed. Different combinations of grid resolution and swap number were tested in order to generate a range of alternative layouts. Examples of the resulting configurations are shown in Figure B.2.

(a) Randomly generated building layout1(*grid cells number* = 6, *swaps number* = 3).

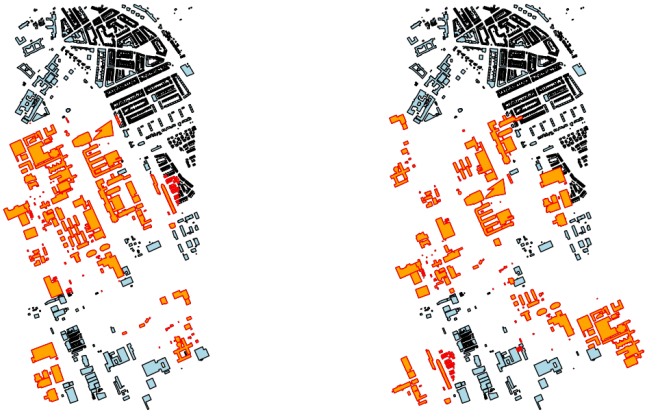

(b) Randomly generated building layout1 (*grid cells number* = 15, *swaps number* = 5).

Figure B.2: Examples of randomly generated building layouts created through grid-cell swapping. The left maps shows the original campus layout and the right panel the modified one, with the relocated buildings highlighted in orange.

However, the resulting layouts exhibited several limitations, as buildings often overlapped, the street structure became unclear and the overall spatial configuration lacked realism.

Because of these limitations, this approach was also considered unsuitable for generating meaningful geometries. This led to the adoption of a more controlled method, based on the manual relocation of groups of buildings, which was then followed in this thesis.